Atmospheric Response to a Collapse of the North Atlantic Circulation Under A Mid-Range Future Climate Scenario: A Regime Shift in Northern Hemisphere Dynamics

Clara Orbe[a,b] , David Rind[a] , Ron Miller[a] , Larissa Nazarenko[a,c] , Anastasia Romanou[a,b] , Jeff Jonas[a,c] , Gary Russell[a] , Maxwell Kelley[a] , and Gavin Schmidt[a]

[a] *NASA Goddard Institute for Space Studies, New York, NY*

[b] *Department of Applied Physics and Applied Mathematics, Columbia University, New York, NY*

[c] *Center for Climate Systems Research, Earth Institute, Columbia University, New York, NY*

Corresponding author: Clara Orbe, clara.orbe@nasa.gov

ABSTRACT: Climate models project a future weakening of the Atlantic Meridional Overturning Circulation (AMOC), but the impacts of this weakening on climate remain highly uncertain. A key challenge in quantifying the impact of an AMOC decline is in isolating its impact, relative to other changes related to increased greenhouse gases. Here we isolate the climate impacts of a weakened AMOC in the broader context of a warming climate using a unique ensemble of SSP 2-4.5 integrations that was performed using the CMIP6 version of the NASA Goddard Institute for Space Studies ModelE (E2.1). In these runs internal variability alone results in a spontaneous bifurcation of the ocean flow, wherein two out of ten ensemble members exhibit an entire AMOC collapse, while the other eight recover at various stages despite identical forcing of each ensemble member and with no externally prescribed freshwater perturbation. We show that an AMOC collapse results in an abrupt northward shift and strengthening of the Northern Hemisphere (NH) Hadley Cell and intensification of the northern midlatitude jet. We then use a set of coupled atmosphere-ocean abrupt CO_2 experiments spanning the range 1-5xCO_2 to show that this response to an AMOC collapse results in a nonlinear shift in the NH circulation moving from 2- to 3xCO_2. Slab-ocean versions of these experiments, by comparison, do not capture this nonlinear behavior. Our results suggest that changes in ocean heat flux convergences associated with an AMOC collapse — while highly uncertain — can result in profound changes in the NH circulation and continued efforts to constrain the AMOC response to future climate change are needed.

1. Introduction

Future projections of the atmospheric circulation remain highly uncertain and reflect uncertainties in the direct radiative response to CO_2 forcing (Deser and Phillips (2009); Grise and Polvani (2014); Shaw and Voigt (2015); Ceppi et al. (2018)), as well as both the (direct) response to changes in sea surface temperatures (SSTs) and the (indirect) response to changes in eddy feedbacks (see Shepherd (2014) and references therein). Among the former, uncertainties in SST projections over the subpolar North Atlantic are particularly consequential, as they strongly influence the location and strength of the North Atlantic storm track, with profound downstream impacts on precipitation and wintertime weather over Europe and parts of Africa (e.g., Zhang and Delworth (2006), Smith et al. (2010), Woollings et al. (2012), O'Reilly et al. (2016)). In particular, while increases in greenhouse gases over the 21st century are expected to result in substantial warming over much of the North Atlantic, climate models project considerable cooling over midlatitudes resulting in a so-called "North Atlantic warming hole (NAWH)" (e.g., Josey et al. (2018), Drijfhout et al. (2012), Robson et al. (2016), Caesar et al. (2018)). While the drivers of this NAWH have been under considerable debate, recent detection-attribution analysis suggests that the anthropogenic signal of the NAWH has emerged from internal climate variability and, moreover, that this cooling can be attributed to declining northward oceanic heat flux over recent decades related to increased greenhouse gas emissions (Chemke et al. (2022)).

Among other mechanisms contributing to the development of the NAWH, the slowdown of the Atlantic Meridional Overturning Circulation (AMOC) has been invoked as one potential key driver (Cheng et al. (2013), Rahmstorf et al. (2015), Menary and Wood (2018)). Studies have long shown that changes in the strength of the AMOC can have widespread impacts not only on other components of the ocean circulation but, more generally, on the broader atmospheric climate system, resulting in a southward shift of the intertropical convergence zone (ITCZ) (e.g., Zhang and Delworth (2005), Vellinga and Wood (2008), Jackson et al. (2015)), a strengthening of the Walker circulation (e.g., Vial et al. (2018), Orihuela-Pinto et al. (2022)) and a northward shift of the Northern Hemisphere (NH) jet stream (e.g., Liu et al. (2020), Bellomo et al. (2021)). Understanding the global scale atmospheric response to changes in AMOC strength is important not only for projections of future climate, but also for understanding paleoclimate records and the dynamics of past Dansgaard-Oeschger events. In particular, while the future collapse of an

AMOC is still considered unlikely, the latest generation of coupled climate models project stronger weakening with future warming, compared to older generations of models (Weijer et al. (2020)).

In addition to its impacts on global precipitation, SST-related changes in the AMOC can change the baroclinicity of the atmosphere, which can result in changes in the storm tracks (Woollings et al. (2012)). However, the precise impacts of a weakened AMOC on atmospheric baroclinity are not well understood, largely because studies have used models that exhibit a wide diversity in the amplitude and spatial extent of the NAWH (Gervais et al. (2019), Haarsma et al. (2015), Menary and Wood (2018)). Nonetheless, despite these uncertainties in the drivers and extent of the NAWH, Woollings et al. (2012) showed that the response of the North Atlantic storm track to climate change was singularly shaped by changes in ocean-atmosphere coupling.

The role of the AMOC in future projections of the jet stream in the Climate Model Intercomparison Project phase 5 (CMIP5) and phase 6 (CMIP6) models was recently examined in Bellomo et al. (2021) (hereafter KB2021), who showed that changes in the AMOC play a primary role in determining the magnitude of the projected poleward displacement of the NH zonal mean jet stream. In particular, by stratifying models according to the strength of their projected AMOC weakening (in response to a quadrupling of CO_2), the authors showed that models with a larger AMOC decline (> 7 Sv, relative to preindustrial values) exhibit minimum warming over the North Atlantic, a southward displacement of the intertropical convergence zone (ITCZ) and a poleward shift of the northern midlatitude jet. The results from KB2021 suggest that the AMOC is a major driver of intermodal uncertainty in future projections of the northern jet stream (and associated hydrological impacts).

A key challenge in quantifying the impact of AMOC uncertainties on future projections of the large-scale atmospheric circulation is in isolating its impact, relative to other changes related to increased greenhouse gases. Thus, while the results from KB2021 are compelling, that study drew conclusions based on the spread among models subject to the same abrupt 4xCO_2 forcing and it is not clear if the models exhibiting greater AMOC weakening were also models that exhibit other characteristics that would independently impact the jet stream. At the same time, previous studies using more traditional freshwater flux perturbations to examine the jet (and other climate) responses to a weakened AMOC, have done so in the absence of other background changes related to increased CO_2 (e.g., Zhang and Delworth (2005), Jackson et al. (2015)). As such, these studies may produce a circulation response to a weakened AMOC that is different than what might occur if other factors impacting atmospheric temperature gradients are included.

One recent attempt to isolate the climate impacts of a weakened AMOC in the broader context of a warming climate was performed in Liu et al. (2020). In that study, the authors compared fully coupled RCP8.5 simulations using a full physics comprehensive model (CCSM4) with identically forced simulations in which a negative freshwater perturbation over the subpolar North Atlantic was added after year 1980 in order to maintain the AMOC strength (while preserving all other forcings). That study showed results that were generally consistent with KB2021, pointing to a major role of the AMOC in causing widespread cooling stretching from NH high latitudes to the tropics and a poleward displacement of the NH midlatitude jet.

While the results from Liu et al. (2020) represent an important step forward in isolating the impacts of the AMOC on the storm tracks in the context of a warming climate, it is not clear that prescribing a negative freshwater perturbation does not potentially interfere with nonlinear components of the AMOC response in a coupled system. To this end, here we present new results featuring an ensemble of SSP 2-4.5 integrations that was performed using the CMIP6 version of the NASA Goddard Institute for Space Studies (GISS) ModelE (E2.1) (Kelley et al. (2020)). In particular, we show results from a subset of the runs documented in Romanou et al. (Under Review) (hereafter AR2022), in which the authors identified a tipping point in the SSP 2-4.5 ensemble occurring during the "extended" portion of the simulations (i.e. beyond year 2090, after which CO_2 emissions are ramped down). During this time period the authors show that internal variability alone results in a spontaneous bifurcation of the ocean flow, wherein two out of ten ensemble members exhibit an entire AMOC collapse, while the other eight recover at various stages (Figure 1a). Note that, in contrast to the aforementioned freshwater hosing studies, in which an AMOC collapse is induced by adding freshwater, in these experiments the AMOC collapse is caused by a reduction in evaporation from the ocean, mediated by sea ice melting (AR2022). As such, the atmospheric configuration that is used to produce this effect in an interactive mode is likely to be very different from an atmosphere which is simply responding to a prescribed freshwater flux perturbation.

Whereas AR2022 focused primarily on the oceanic conditions giving rise to this divergence in AMOC behavior among different ensemble members, here we focus on the subsequent impacts this has on the atmospheric large-scale circulation. In particular, we contrast the behavior between two and eight ensemble members in which the AMOC respectively collapses and recovers to historical values by year 2400 (red vs. green lines, Fig. 1a). As such, we isolate the impact of a weakened AMOC on the atmospheric circulation in the presence of increased greenhouse gas warming using a single model (unlike KB2021) and without any need to invoke negative freshwater perturbations (as in Liu et al. (2020)). To the best of our knowledge, this represents the first time that the AMOC imprint on the circulation has been isolated in the context of background increases in greenhouse gases using a fully coupled comprehensive model, absent any externally imposed freshwater perturbations that may potentially interfere with the model's internal dynamics.

As discussed in AR2022, the ensemble members in which the AMOC collapses are substantially cooler than those runs in which it recovers, with wintertime global mean surface temperature (GMST) differences of about 1°C by year 2400 (Fig. 1c). Therefore, in documenting the influence of the AMOC on the atmosphere in the different SSP 2-4.5 ensemble members it is natural to ask how the large-scale thermodynamic and dynamical circulations scale with these differences in GMST. Though perhaps naive, it is common practice to assume that the climate system scales linearly with GMST, as reflected in the use of so-called "global warming levels" in the recent IPCC AR6 report (James et al. (2017)) and the widely applied related practice of "pattern scaling" (e.g., Santer et al. (1990), Tebaldi and Arblaster (2014)). Recent studies, however, have shown that the climate's so-called "dynamical sensitivity" – in particular, circulation shifts associated with changes in the Hadley Cell and storm tracks - do not scale with equilibrium climate sensitivity (Grise and Polvani (2016), Ceppi et al. (2018)). As those studies, however, focused on large (CMIP5) multi-model ensembles, it is not clear if similar conclusions also apply to single models and to climate states in which the AMOC has undergone a substantial weakening. More precisely, it remains unclear how much of the circulation response to a weakened AMOC is related simply to changes in GMST or, rather, to changes in (free-tropospheric) meridional temperature gradients away from the surface.

To this end, in addition to reporting on the results from the SSP 2-4.5 ensemble we also examine a suite of abrupt 1-5xCO_2 experiments that were conducted using the same model version (Mitevski et al. (2021)). In particular, we exploit the fact that between 2- and 3xCO_2 abrupt forcing the AMOC respectively recovers and collapses by year 150 (Fig. 1b), behavior which is generally

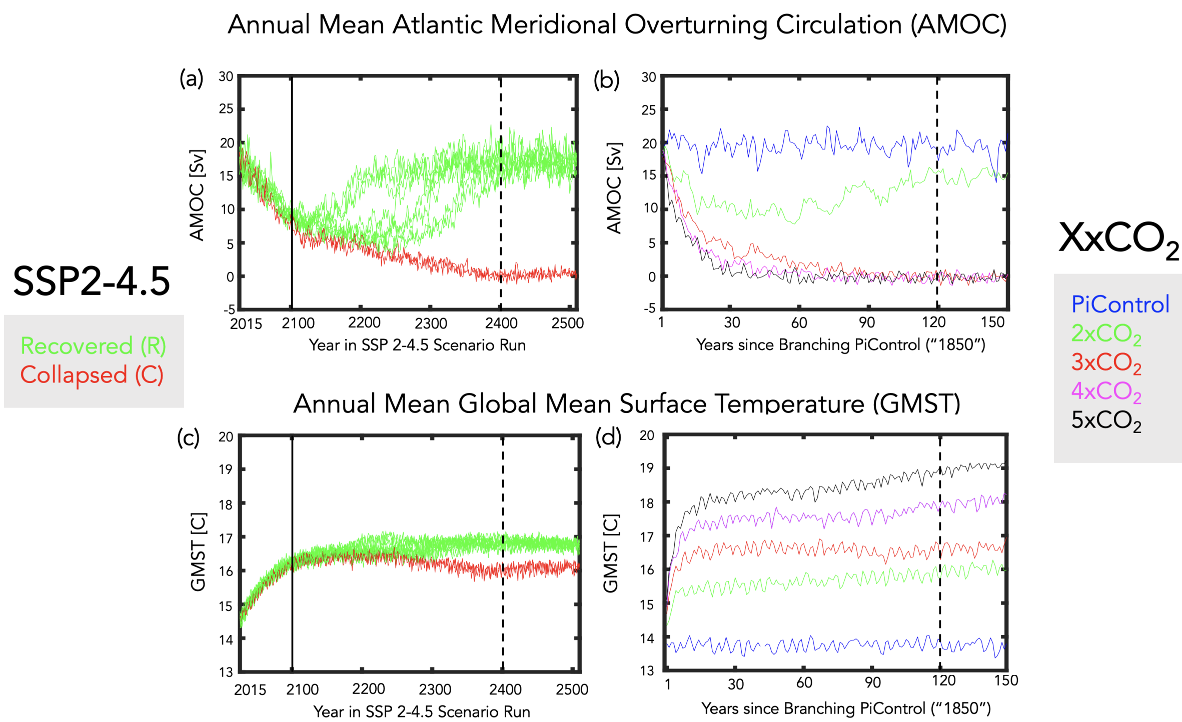

FIG. 1. Top: Evolution of the annual mean maximum overturning stream function in the Atlantic ocean, evaluated at 48°N, compared among the SSP 2-4.5 (8) recovered and (2) collapsed ensemble members (top, left) and among the abrupt XxCO$_2$ runs (top, right). Bottom: Same as top panels, except showing annual mean global surface temperature (GMST). Vertical solid lines mark the beginning of the "extension" portion of the SSP 2-4.5 scenario. Vertical dashed lines indicate the years after which climatological averages are evaluated (i.e., years 2400-2500 (left) and years 120-150 (right))

.

similar to the differences in AMOC behavior between the recovered and collapsed members of the SSP 2-4.5 ensemble, hereafter referred to as SSP 2-4.5 R and SSP 2-4.5 C, respectively (Fig. 1a). However, by spanning a much broader range of GMST responses, compared to the SSP 2-4.5 ensemble – and assuming that the atmospheric responses to an AMOC collapse are similar between the 3xCO$_2$ and SSP 2-4.5 collapsed ensemble members (a point which we examine in Section 3a3) – the broader set of XxCO$_2$ experiments affords a unique opportunity to investigate the relationship between dynamical and equilibrium climate sensitivity in the presence of a collapsed AMOC.

In Section 3 we begin by contrasting the large-scale atmospheric circulation responses between the SSP 2-4.5 R and C members in which the AMOC recovers and remains collapsed after year 2400 (Sections 3a1-2, Q1 below). We then compare this behavior with the circulation differences with the 2xCO_2 and 3xCO_2 integrations (Section 3a3, Q2). After showing that the 3xCO_2 circulation changes in the NH are largely dominated by the behavior of the AMOC, we then further use the broader set of 1-5xCO_2 abrupt experiments to examine how the collapse of the AMOC modulates the relationship between the NH dynamical circulation and GMST over a much broader range of CO_2 forcing (Section 3b, Q3). In addressing the latter we also use slab-ocean model integrations in order to examine if the behavior exhibited in the coupled atmosphere-ocean runs is reflected in simulations in which ocean heat flux convergence changes associated with an AMOC collapse are not allowed to occur.

The main goals of the manuscript are centered around addressing these three questions:

Q1) How does a collapse of the AMOC influence the atmospheric circulation in the presence of the same background CO_2 forcing (SSP 2-4.5 ensemble)?

Q2) How does this compare with the response to an AMOC collapse induced by different CO_2 forcing (2xCO_2 vs. 3xCO_2)?

Q3) Are AMOC-related circulation changes mediated primarily by GMST or by changes in atmospheric temperature gradients?

In addressing Q1-Q3 we show that the AMOC tipping point described in AR2022 results in a vastly different atmospheric response between ensemble members in which the AMOC collapses versus members in which the AMOC recovers. In particular, in our model the atmospheric response to an AMOC collapse (occurring on the timescales addressed in this study) reflects a regime shift between a climate state in which the NH Hadley Cell and midlatitude jet are substantially weaker and displaced further equatorward (strong AMOC) compared to a state in which they are substantially stronger and displaced poleward (weak AMOC).

2. Analysis/Methods

a. Models and Experiments

Here we use simulations from two sets of experiments produced using the GISS version E2.1 climate model (GISS-E2-1-G) (Kelley et al. (2020)), which consists of a 40-level atmospheric model with a horizontal resolution of 2^{o} x 2.5^{o} latitude/longitude coupled to the 1^{o} horizontal resolution 40-level GISS Ocean v1 (GO1) model (for more details of GO1 see AR2022). Comprehensive reviews of this model's response to historical and future climate change simulations are provided in Miller et al. (2021) and Nazarenko et al. (2022), respectively.

We first examine results from the SSP 2-4.5 ensemble that contributed to the official submission of the NASA-GISS climate group to CMIP6. In particular, we contrast the behaviors of eight members in which the AMOC has recovered by year 2400 (SSP 2-4.5 R) with two members in which it has remained collapsed (SSP 2-4.5 C) (Fig. 1a). As discussed in AR2023, this contrasting behavior emerges during the "extension" portion following year 2090, beyond which CO_2 concentrations slow down in growth from 597 ppm to 643 ppm at year 2200 and decline thereafter (Meinshausen et al. (2020)). That study further showed that the divergence in the behavior of the AMOC results from stochastic variability associated with sea-ice transport and melting in the Irminger Sea that led to a reduction in evaporation and salinity. Note that, whereas AR2023 was primarily focused on identifying the mechanisms leading to different recovery times among the SSP 2-4.5 R, our interest is in quantifying the impact of an AMOC collapse on the large-scale circulation after year 2400. To this end, we treat the SSP 2-4.5 R and C simulations as comprising two distinct "recovered" and "collapsed" ensembles.

To put the SSP 2-4.5 results in a broader context, we also examine the coupled atmosphere-ocean 1-5xCO_2 abrupt CO_2 experiments reported in Mitevski et al. (2021), which were performed using the same version of the model. We restrict our attention to a subset of the runs, focusing mainly on the 2- and 3xCO_2 runs, but also including results from the 4- and 5xCO_2 simulations when commenting on the linearity of the atmospheric circulation responses with respect to changes in GMST (Section 3b). As shown in Figure 1, the behavior of the AMOC by the end of the abrupt 2- and 3xCO_2 runs is generally very similar to the AMOC behavior in the SSP 2-4.5 R and C ensemble members, respectively, past year 2400. This similar behavior also appears at lower latitudes (26^{o}N) (not shown), consistent with the findings in AR2022, who showed a strong correlation in AMOC strength at these two latitudes (0.97) within the broader SSP 2-4.5 ensemble.

In addition to the results from the fully coupled ocean-atmosphere model (hereafter FOM) SSP 2-4.5 and XxCO_2 integrations, we also show results from q-flux or slab-ocean model (SOM) integrations spanning the range 1-5xCO_2. In these experiments any changes in ocean horizontal heat transport and vertical heat uptake by the deep ocean are not included as the ocean heat flux convergences in the mixed layer ($-\nabla\cdot(vT)$, including both horizontal and vertical heat fluxes) are calculated using preindustrial control values. At the same time, the SOM experiments do capture the mixed layer temperature changes resulting from changes in the net surface heat fluxes (hereafter referred to as "thermodynamic" ocean coupling). As such, contrasting the responses in the FOM and SOM experiments isolates the role of dynamic (i.e. ocean heat flux convergence) coupling on the atmospheric responses in the FOM simulations, consistent with the presentation in Chemke et al. (2022). Note that this approach does not explicitly isolate the contribution of changes in SSTs to the atmospheric circulation response, as the SST response reflects both changes in thermodynamic and dynamic ocean-atmosphere coupling. However, robustly isolating the impact of SSTs can be tricky as previous studies utilizing prescribed SST "warming hole" patterns have shown large sensitivity to how these patterns are prescribed, particularly in relation to SST gradients (see discussion in Gervais et al. (2019)).

b. Temporal Averaging and Spatial Domains

To compare the atmospheric responses from the SSP 2-4.5 simulations with those from the abrupt CO_2 experiments we focus on climatological averaging periods during which the characteristics of the AMOC are similar, i.e., years when the AMOC has recovered in the 2xCO_2 and SSP 2-4.5 R runs, while the AMOC has remained collapsed in the 3xCO_2 and SSP 2-4.5 C experiments. As indicated in Figure 1 (dashed black vertical lines) this corresponds to years beyond which the maximum value of the overturning stream function at 48^{o}N has reached nearly zero, corresponding to years 120-150 and 2400-2500 in the XxCO_2 and SSP 2-4.5 integrations, respectively. We refer to these periods hereafter as the "equilibrated" responses in the model, bearing in mind that the AMOC exhibits multi-centennial instability as was illustrated in an older version of the GISS climate model (Rind et al. (2018)). Variations on these longer timescales are not addressed in this study.

We begin by presenting differences in climatological means between the SSP 2-4.5 R and C ensembles and between the 2xCO_2 and 3xCO_2 integrations. Statistical significance of the SSP 2-4.5 C-R differences is assessed using a Welch's t-test, given the unequal sample sizes represented by the 8-member R and two-member C ensembles. A two-sample Student's t-test is used when comparing the abrupt CO_2 responses. In addition, when putting the SSP 2-4.5 results in the context of the broader 1-to-5xCO_2 forcing range we define all responses relative to a 150-year average over the preindustrial control simulation from which the abrupt CO_2 experiments are "branched".

For the majority of the analysis considered here we focus on December-January-February (DJF) and over the NH. Our focus on DJF is consistent with the presentation in AR2022, while our focus on the NH is motivated by Mitevski et al. (2021), who showed that the AMOC collapse occurring between 2- and 3xCO_2 results in a non-monotonic response in global mean surface temperature, driven primarily by changes occurring in the NH (more precisely, the North Atlantic). We deviate from this convention, however, at two different points in this study. First we use annual mean GMST when evaluating the dynamical sensitivity scaling in Section 3b; second, we present the energy budget analysis in Section 3c using annual means in order to facilitate comparison with previous studies. Some results about the Southern Hemisphere (SH) circulation response are also presented, but only discussed briefly.

Finally, while our main focus is on the "equilibrated" responses defined above, we are also interested in exploiting the evolution of the responses, as in Grise and Polvani (2017) and Chemke and Polvani (2019). As shown in those studies, consideration of the response timescales of different variables affords unique insight into possible mechanisms governing their evolution.

c. Scaling with Global Mean Surface Temperature (GMST)

We begin by comparing the absolute differences in the atmospheric "equilibrated" responses between the SSP 2-4.5 R and C members (Section 3a1-2) and between the 2-and 3xCO_2 simulations (Section 3a3). When interpreting these differences, however, it is important to note that these could partly be reflective of background differences in the CO_2 forcing. In particular, the CO_2 values in the SSP 2-4.5 extended experiments peak at 643 ppm, or roughly 2.4 times preindustrial values, and decrease thereafter (see Figure 1a in AR2022). It is perhaps not surprising, therefore, that this value of CO_2 lies in between the 2- and 3xCO_2 levels identified in Mitevski et al. (2021) as the transition point between the AMOC recovering and collapsing under abrupt forcing (Figure 1a).

Given these differences in CO_2 forcing (further exaggerated when considering the broader suite of 1-5xCO_2 experiments) it may seem most natural to compare the simulations with respect to their associated instantaneous radiative forcing (RF) as in Mitevski et al. (2021). However, another difference between the transient SSP 2-4.5 and abrupt 1-5xCO_2 experiments is the evolution of the forcing. As the AMOC is known to be sensitive to the time history of the forcing, this is important to take into consideration, and so we cast our scaling analysis in Section 3b (in which the SSP 2-4.5 results are compared against the broader 1-5xCO_2 suite) in terms of GMST. This approach is also more in spirit with Ceppi et al. (2018) as it directly addresses the extent to which the dynamical sensitivity captured in the simulations scales with equilibrium climate sensitivity (Q2).

Finally, a related but distinct approach is to normalize by annual mean GMST. KB2021 showed that doing so highlights large differences in temperature gradients and the zonal mean meridional circulation between models in which the AMOC weakens substantially (> 7 Sv), compared to models showing a limited AMOC response (< 7 Sv). However, while this approach is well suited to understanding the multi-model response to the same (4xCO_2) forcing, it does not directly afford insight into how dynamical sensitivity scales with GMST. As we have tried both normalizing and not normalizing in this study and draw generally very similar conclusions (not shown), we focus on the unnormalized results.

d. Analysis Approach

1) Hadley Cell and Storm Track Diagnostics

Whereas KB2021 focused on the latitude of the northern midlatitude jet, here we expand their analysis to also include measures of the Hadley Cell (HC) and the storm tracks. Figure 2a highlights how these measures of the HC and midlatitude jet are coupled through eddy momentum fluxes.

To quantify the characteristics of the Hadley Cell we use metrics calculated using the Tropical-width Diagnostics (TropD) code (Adam et al. (2018)) based on fields that were zonally and seasonally averaged before calculation of the metrics. The edge of the HC, ϕ_{UAS}, is defined as the zero-crossing latitude of the surface zonal wind (corresponds to UAS in TropD and is calculated

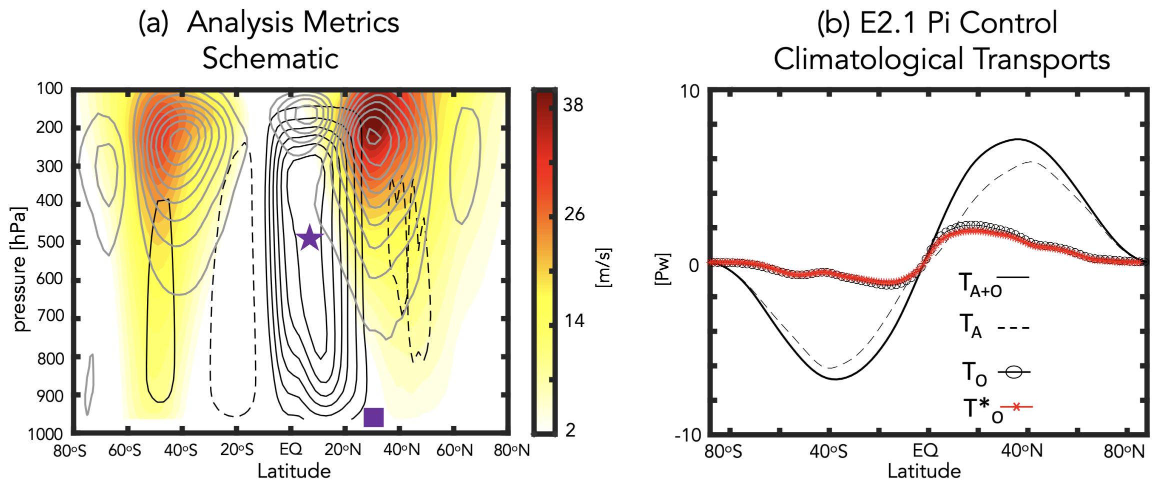

FIG. 2. (a): Schematic of the main zonal mean dynamical metrics considered in this study, illustrated using data from the preindustrial control simulation. The December-January-February (DJF) climatological mean meridional circulation is shown in black contours, with solid and dashed lines denoting clockwise and counterclockwise directions, respectively (contour interval: $3\text{x}10^{10}$ kg/s). The DJF zonally averaged zonal winds are shown in the filled colored contours (only positive values shown; contour interval: 2 m/s) and the DJF eddy momentum fluxes are shown in the grey contours (contour interval: 8 m^2/s^2). The purple star denotes the Northern Hemisphere (NH) Hadley Cell strength, or the maximum value of the mean meridional streamfunction at 500 hPa equatorward of where it crosses zero, while the edge is denoted by ϕ_{UAS} (purple square), or the zero-crossing latitude of the surface zonal wind. (b): Annual mean meridional distributions of the total atmospheric (T_A; black dashed line) and combined atmosphere-ocean (T_{A+O}; black solid line) northward energy transports for the preindustrial control simulation. The implied ocean heat transport (T_O; black circled line), calculated by subtracting T_A from T_{A+O}, exhibits good agreed with online calculations of the ocean transports (T^*_O; red starred line). For more details see Section 2.

using the "zerocrossing" method) (Fig. 2a, purple square). This measure of the HC was shown to correlate well with the latitude at which the mean meridional streamfunction at 500 hPa crosses 0 poleward of its tropical extremum (Waugh et al. (2018)). The value of that tropical extremum (Ψ_{500}) is also examined as a measure of HC strength (Fig. 2a, purple star).

In addition to looking at the Hadley Cell, we also examine its relation to the northern midlatitude jet via the eddy momentum fluxes. This is based on research showing a strong connection between the evolution of the Hadley Cell and the latitude of the maximum eddy momentum fluxes

(Schneider (2006); Chemke and Polvani (2019); Menzel et al. (2019)). The eddy momentum fluxes are calculated as in Chemke and Polvani (2019) as the time mean of [u'v'], where u and v are the zonal and meridional winds, respectively, and primes represent deviations from both the zonal and monthly means. In particular we are interested in the latitude where the eddy momentum flux maximizes (eddy momentum convergence = 0) (Fig. 2a, grey contours). As it is well known that the largest eddy momentum flux convergences are closely collocated with the extratropical storm tracks (e.g., Lau et al. (1978), Lim and Wallace (1991)), we also examine the vertically averaged eddy kinetic energy, calculated using daily output. Connections with static stability and baroclinic eddy generation are also made, where the latter is quantified using $\sim \alpha' \omega'$, where primes denote zonal deviations and α and ω refer to one over the density and vertical velocity in pressure coordinates, respectively.

2) Energetic Analysis

To put the results of the dynamical analysis in an energetic context we evaluate the total meridional heat transport of the coupled ocean-atmosphere transport system, further partitioned into its oceanic and atmospheric contributions. Following Magnusdottir and Saravannan (1999) we estimate the total vertically integrated atmospheric heat flux ($\mathrm{T_A}$) as:

$$\frac{\partial cos\phi}{acos\phi\partial\phi}\overline{[\mathrm{T_A}]} \equiv \frac{\partial cos\phi}{acos\phi\partial\phi}\int_1^0 \overline{(c_pT+gz+Lq)v\rho d\eta}$$

$$= \overline{[-\mathrm{F_T}-\mathrm{F_S}+\mathrm{SHF}+\mathrm{LHF}]} \qquad (1)$$

as well as the vertically integrated meridional heat flux in the combined atmosphere-ocean system ($\mathrm{T_{A+O}}$) as:

$$\frac{\partial cos\phi}{acos\phi\partial\phi}\overline{[\mathrm{T_{A+O}}]} \equiv \overline{[-\mathrm{F_T}]} \qquad (2)$$

where moist static energy density is the sum of dry static energy density (c_pT+gz) and the latent heat density (Lq), ρ and v refer to the mass density and horizontal velocity on η surfaces. Zonal averages and time averages are denoted by square brackets and overbars, respectively. The terms on the RHS of both equations refer to energy fluxes out of the top of the atmosphere and at the surface: F_T (net upward flux of radiation at the top of the atmosphere, calculated as outgoing longwave radiation (OLR) minus the absorbed solar radiation (ASR)), F_S (net downward flux of radiation at the surface equal to the sum of net downward longwave (LWF) and shortwave (SWF) radiation), and the fluxes of latent and sensible heat at the surface (LHF and SHF).

The resulting annual mean meridional distributions of T_A and T_{A+O}, calculated using the E2.1 150-year preindustrial control simulation, is consistent with the climatological energy transports presented in other studies (e.g., Magnusdottir and Saravannan (1999), Held and Soden (2006)) (Figure 2b). Note that the implied ocean heat transport, calculated by subtracting the first from the second equation above (Fig. 2b, black circled line) is found to exhibit good agreement with online calculations of the ocean transports (Fig. 2b, red starred line). These northward ocean heat transports, simulated in historical integrations using E2.1, have been shown to agree well with 1992-2011 estimates from the ECCO ocean state estimate (see Figure 23 in Kelley et al. (2020)). Finally, in addition to examining the compensation between atmospheric and oceanic poleward transports, we also further partition T_A into its moist versus dry contributions using online calculations of the vertically integrated dry static energy and latent heat northward transports (Section 3c).

3. Results

We begin by contrasting the regional SSP 2.45 R and SSP 2.45 C responses in sea surface temperatures, sea level pressure, precipitation and zonal winds in Section 3a1 and in the large-scale zonal mean circulation (Section 3a2). Then we compare the SSP 2.45 C-R differences to the differences between the $2xCO_2$ and $3xCO_2$ simulations (Section 3a3), further placing these results in the context of the broader $1\text{-}5xCO_2$ forcing by examining how changes in various thermodynamical and dynamical quantities scale with changes in global mean surface temperature (Section 3b). To interpret the dynamical scaling results we then examine the compensation that arises between the ocean and atmosphere in response to the shutdown of the AMOC (Section 3c).

a. Equilibrated Responses

1) SSP 2-4.5 Collapsed vs. Recovered: Near-Surface Temperatures, Precipitation and Winds

Figure 1 (bottom panels) shows the evolution of annual global mean surface temperature in the SSP 2-4.5 C and R members (Fig. 1c) and the abrupt CO_2 experiments (Fig. 1d). Comparing the collapsed versus recovered SSP 2-4.5 ensemble members reveals global cooling in response to a collapse of the AMOC such that by the time that the AMOC has recovered in SSP 2-4.5 R the annual mean global surface temperature is almost one degree warmer, relative to the SSP 2-4.5 C members. In the abrupt CO_2 simulations, the GMST change in the 3xCO_2 experiment is only 0.6^{o}C warmer than the 2xCO_2 simulation, reflective of a clear flattening of the warming trend after years ~60-70. Overall, the changes in GMST are 2.2^{o}C, 2.8^{o}C, 3.0^{o}C, and 2.3^{o}C for the 2xCO_2, 3xCO_2 and SSP 2-4.5 recovered and SSP 2-4.5 collapsed ensembles, respectively.

That the cooling associated with a steady decline and eventual collapse of the AMOC acts to mitigate, and partially counteract, other components of the global surface temperature change is reflected in a non-monotonic change in equilibrium climate sensitivity that occurs between 2- and 3xCO_2 over the broader range of experiments spanning 1-to-5xCO_2 (see Figure 1 in Mitevski et al. (2021)). This counteracting of warming due to a weakening of the AMOC has also been shown to occur in 21st century warming simulations (Drijfhout et al. (2012), Caesar et al. (2018), Marshall et al. (2015)).

While the AMOC influence on the climate can occur via its changes in GMST, a reduction in AMOC strength can also influence sea surface temperature patterns. We examine this next, with a focus on DJF, and examine changes in SSTs and associated meridional and zonal gradients over the Atlantic and Pacific (Figure 3a). Note that a saturated color bar has been used in order to highlight the structure of SST changes outside of the North Atlantic region.

Examining first the North Atlantic we find much more cooling occurring in the SSP 2-4.5 collapsed simulations (Fig. 3a) over the subpolar North Atlantic (SPNA), consistent with the results from previous studies. This cooling that occurs within the SPNA region is also associated with a large increase in meridional SST gradients over the North Atlantic south of 40^{o}N. Zonally, gradients are also enhanced over the Gulf Stream between the western and eastern Atlantic basins. There is also an indication of a slight increase in SST gradients in the tropics.

The cooler SSTs in the recovered simulations are not only confined to the Atlantic, but also span the Pacific (Fig. 3a), resulting in stronger meridional SST gradients, particularly over middle northern latitudes. Preliminary analysis of the evolution of the SST response (Appendix Figure 1) shows that this cooling over the extratropical Pacific takes several centuries to fully realize itself and may be related to a deepening and poleward shift of the Aleutian Low (Fig. 3c), resulting in more advection of colder temperatures over the West Pacific (Wu et al. (2008)), although direct thermodynamic advection of colder North Atlantic air may also be occurring. By comparison, the changes in SSTs and associated gradients in the tropical Pacific are much smaller. Unlike some previous studies (Timmermann et al. (2007), Zhang and Delworth (2005)) we find no evidence of an El Niño like response to an AMOC weakening, although the robustness of this response has recently been put into question (KB2021).

In the SH, SSTs warm over the extratropics in the SSP 2-4.5 collapsed integrations, compared to the simulations in which the AMOC recovers. This warming takes several centuries to develop (Appendix Figure 1) and resembles the evolution of the SST pattern documented in previous studies (see Figure 7 in Pedro et al. (2018)). This delayed warming over the SH results in increased SST gradients over the South Atlantic (~60^{o}S) in the SSP 2-4.5 C runs, relative to SSP 2-4.5 R, a feature which is not captured in the 3xCO_2 simulation (discussed more in Section 3a3).

In addition to the changes in SSTs, the response in precipitation in the SSP 2-4.5 collapsed simulations reflects large decreases over the North Atlantic subpolar region, reductions over the Amazon and suggestions of a southward shift of the ITCZ over both the Atlantic and East Pacific basins (Fig. 3b). By comparison, the increased precipitation in the West Pacific is not statistically significant, consistent with previous studies (Vellinga and Wood (2008), KB2021).

Moving next to more dynamical measures, we examine changes in sea level pressure and near-surface zonal winds (Fig. 3c,d). The changes in sea level pressure show differences over the North Atlantic indicative of enhanced (anticyclonic) high level pressure over the subpolar latitudes in the runs in which the AMOC collapses (Fig. 3c). In addition to these SLP changes over the Atlantic, there is also a pronounced dipole of increased and reduced sea level pressure values over the North Pacific middle and high latitudes. While this response was not discussed in KB2021, earlier studies have shown that a weakening of the AMOC is associated with a deepening of the Aleutian Low (Wu et al. (2008), Liu et al. (2020)).

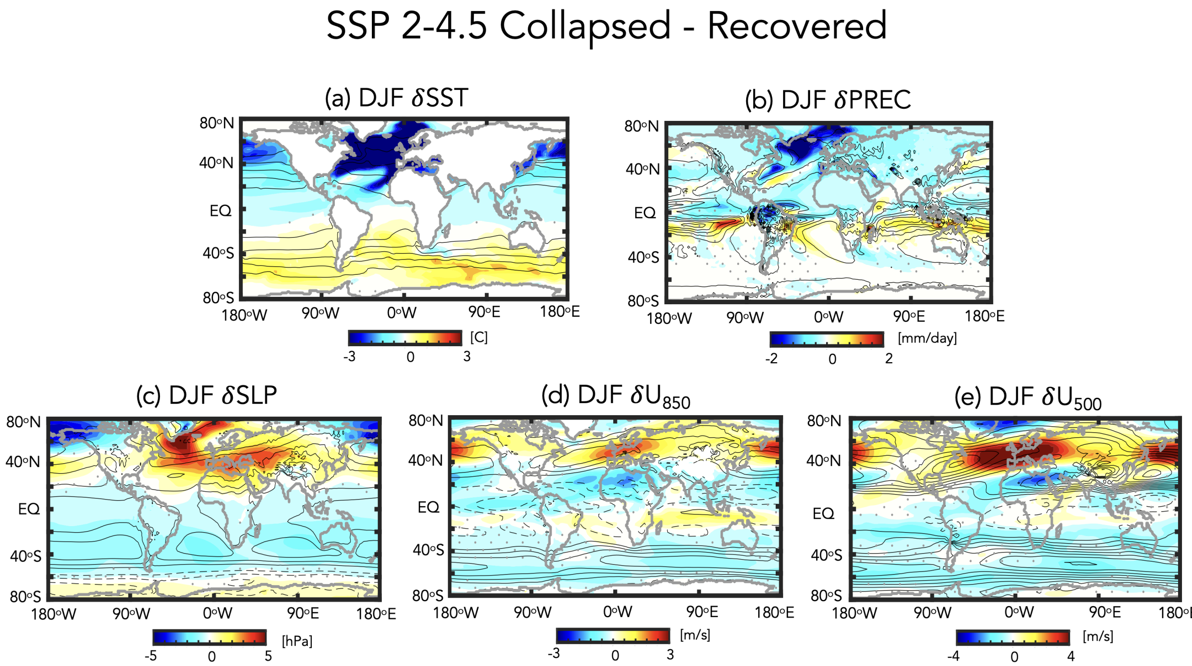

FIG. 3. The difference in the year DJF 2400-2500 climatological mean (a) sea surface temperatures (δSST), (b) precipitation (δPREC), (c) sea level pressure (δSLP), (d) 850 hPa zonal winds (δU_{850}) and (e) 500 hPa zonal winds (δU_{500}) between the SSP 2-4.5 collapsed (C) and recovered (R) ensemble members. Climatological mean values from the preindustrial control simulation are denoted in the black contours (contour intervals: (a) 5^{o}C, (b) 2 mm/day, (c) 5 mb, (d) 3 m/s and (e) 3 m/s). Grey stippling denotes regions where the SSP 2-4.5 C-R differences are not statistically significant.

Consistent with the SLP pressure changes over the North Pacific, there is a strong signature in the near surface zonal winds (850 hPa) (Fig. 3d). While over the Pacific the wind changes more reflect a poleward shift of the midlatitude jet, over the North Atlantic the jet accelerates and extends further eastward over Europe. This acceleration over the North Atlantic is more pronounced in the mid-troposphere (Fig. 3e), as was also reported in KB2021 who identified a statistically significant strengthening of the midlatitude jet in models featuring a stronger AMOC decline at 250 hPa, but not at 850 hPa. Finally, in contrast to the NH, there is a uniform weakening of the zonal winds over the SH extratropics. We discuss the vertical coherence of these wind changes in the next section.

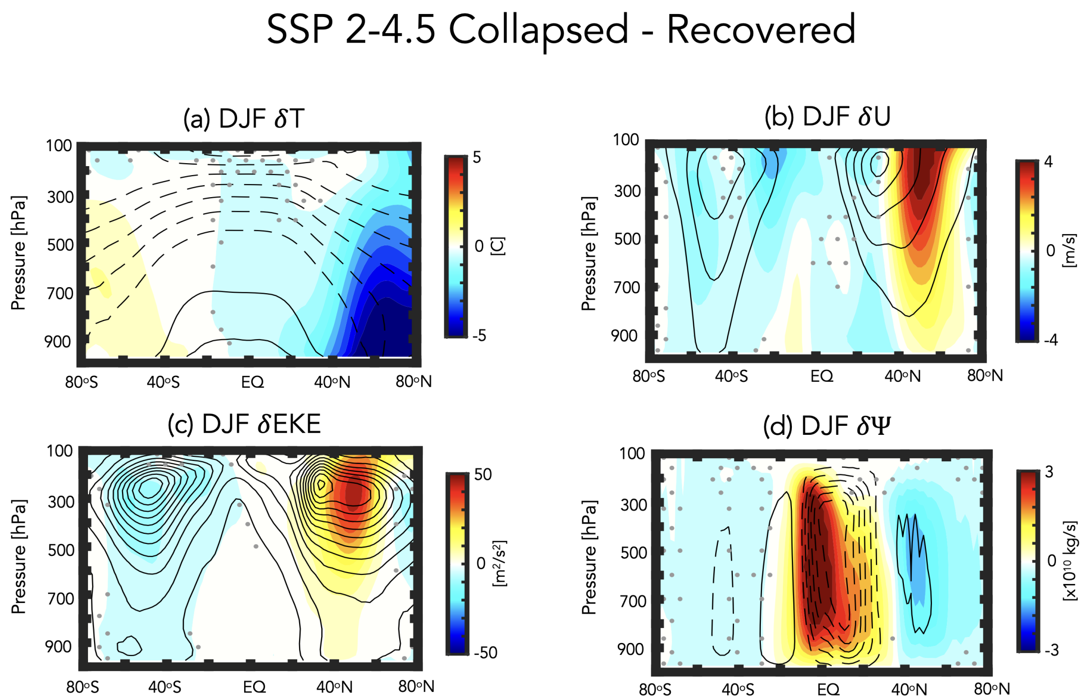

FIG. 4. The difference in the year DJF 2400-2500 climatological mean zonal mean (a) temperature (δT), (b) zonal wind (δU), (c) eddy kinetic energy (δEKE) and (d) Eulerian mean stream function ($\delta\Psi$) between the SSP 2-4.5 collapsed (C) and recovered (R) ensemble members. Climatological mean values from the preindustrial control simulation are denoted in the black contours (contour intervals: (a) 10°C, (b) 8 m/s, (c) 28 m^2/s^2 and (d) 3×10^{10} kg/s). Note that in (d) solid and dashed lines denoting clockwise and counterclockwise directions, respectively. Grey stippling denotes regions where the SSP 2-4.5 C-R differences are not statistically significant.

2) SSP 2-4.5 Collapsed vs. Recovered: Vertical Structure

In addition to its impacts on SSTs, changes in the AMOC impact the vertical structure of meridional temperature gradients in the atmosphere. To interpret the zonal wind changes shown in Figure 3 we therefore next examine the zonal mean changes in temperatures, zonal winds and eddy kinetic energy, as well as their coupling to responses in the tropical mean meridional circulation (Figure 4).

We begin by examining changes in temperature (Fig. 4a), which show much more cooling over the NH high latitude troposphere in the SSP 2-4.5 collapsed runs. A similar reduction in Arctic warming was reported in the "strongly" collapsed model ensemble examined in KB2021 (Figure S5) and in Liu et al. (2020) (Figure 6). In addition to the changes over the northern extratropics,

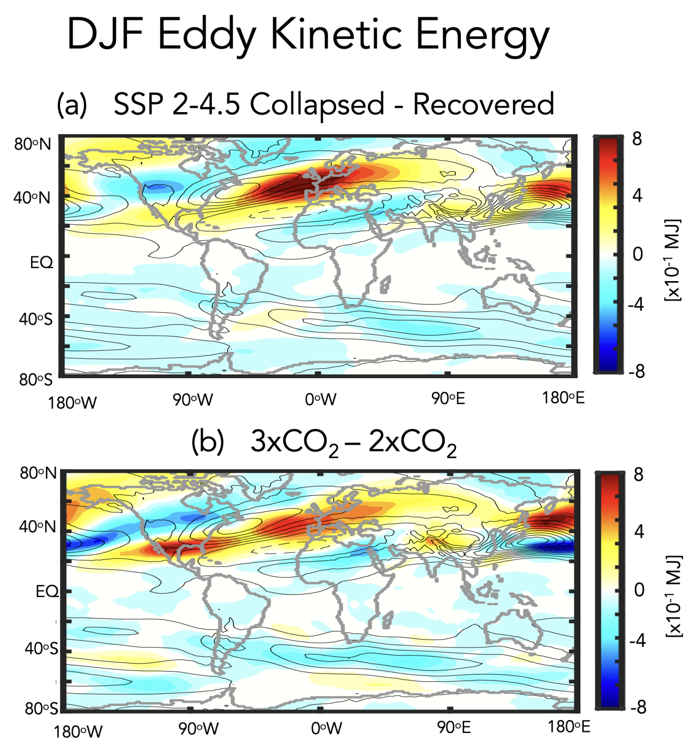

FIG. 5. (a) The difference in the year DJF 2400-2500 climatological mean vertically integrated eddy kinetic energy between the SSP 2-4.5 C and R ensembles. (b) Same as in (a), except showing the difference between the $3xCO_2$ and $2xCO_2$ integrations. Climatological mean values from the preindustrial control simulation are denoted in the black contours (contour interval: $5x10^{-1}$ MJ).

we also find an indication of weak polar amplification characterized by warming throughout the SH middle and high latitudes poleward of 40°S, also seen in the SST differences (Fig. 3a). This warming in the SH is consistent with Liu et al. (2020) (see their Figure 6), but inconsistent with KB2021 who, in addition, identified more warming occurring in the tropical upper troposphere, a feature that is not evident in the SSP 2-4.5 collapsed runs. Normalization of our results by GMST (not shown) produces an anomalous upper tropical tropospheric warming, suggesting that the results reports in KB2021 are reflective not of absolute differences in the temperature response but, rather, of the normalization performed in that study. In addition, in the SH the different temperature response compared to KB2021 also likely reflects their use of shorter (150-year-long) integrations.

Moving next to the zonal winds (Fig. 4b) we find that the reduced warming over NH high latitudes is associated with enhanced meridional temperature gradients, which result in a poleward shift of the zonal mean northern midlatitude jet in the runs in which the AMOC collapses. A similar poleward shift in the NH jet was documented in KB2021 (see their Figure 4) and in Liu et al. (2020). In the SH the zonal winds weaken and, if anything shift equatorward, in the SSP 2-4.5 C ensemble members, consistent with the weak polar amplification in that region (Fig. 4a). Again, this wind response is highly consistent with Liu et al. (2020), but opposite to that shown in KB2021, who identified a poleward shift of the SH jet, consistent with the different meridional temperature gradient response identified in that study. As that study did not propose a testable mechanism for the SH jet changes, it is not entirely clear what is the driver of the differences between their results and those presented here and in Liu et al. (2020), although both the normalization by GMST as well as the differing integration lengths likely contribute.

In concert with the changes in the zonal winds, the changes in eddy kinetic energy (EKE) over the NH feature increases north of 40^{o}N (Fig. 4c). Note that there is no statistically significant response in the subtropics and only the wind (and EKE) changes poleward of 40°N are robust. Zonally, the increases in EKE are concentrated over the North Atlantic and extend eastward over Europe, and well as over the West Pacific (Fig. 5a), strongly resembling the zonal wind changes at 500 hPa (Fig. 3e). Comparisons with the changes in EKE associated with an AMOC collapse in another model (the Community Earth System Model (CESM-LE)) examined in Mitevski et al. (2021) show very similar anomalies (not shown). Furthermore, a spectral decomposition of these NH EKE changes show increased wave energy over wavenumbers 1-6 (primarily in the zonal mean kinetic and available potential energy terms) in the collapsed SSP 2-4.5 members, relative to the recovered members (also not shown).

Finally, the changes in the mean meridional stream function indicate an overall strengthening of the wintertime NH Hadley circulation in the collaped SSP 2-4.5 simulations (Fig. 4d). This intensification of the NH Hadley circulation in response to an AMOC shutdown has been reported in previous studies (Zhang and Delworth (2005), Orihuela-Pinto et al. (2022)) and generally associated with a southward displacement of the ITCZ, although Brayshaw et al. (2009) also identify a zonally localized enhancement of the Hadley Cell region over the subtropical Atlantic, which they associate with increased meridional SST gradients in that region. Compared to those studies, however, our results also show a poleward displacement of the northern Hadley Cell edge in the lower troposphere (>500 hPa), a result which has not been directly commented on in the

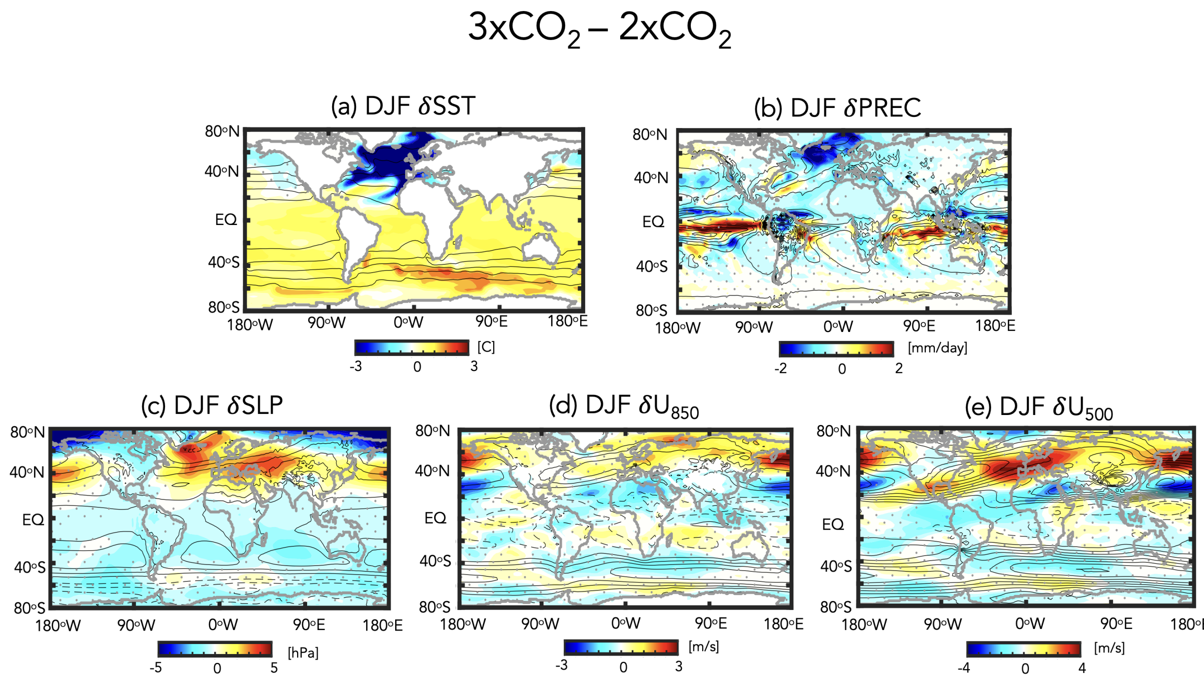

FIG. 6. Same as Figure 3, except showing the difference between the year 120-150 climatological mean $3xCO_2$ and $2xCO_2$ responses.

literature. These stream function anomalies over the NH extratropical lower troposphere appear to be coupled to a slight strengthening and poleward displacement of the northern Ferrel cell.

3) Comparison with $2xCO_2$ vs $3xCO_2$

Comparisons of the surface and lower tropospheric impacts associated with an AMOC collapse in the SSP 2-4.5 ensemble (Fig. 3) with those moving from 2- to $3xCO_2$ (Fig. 6) reveal a high degree of consistency. In particular, over the North Atlantic the changes moving from $2xCO_2$ to $3xCO_2$ reflect much stronger cooling of SSTs (Fig. 6a), reduced precipitation (Fig. 6b) and an anomalous anticylonic circulation over the North Atlantic subpolar gyre region (Fig. 6c), as well as a strengthening and eastward extension of the North Atlantic jet over Europe (Fig. 6d, 6e). The magnitude of these changes is similar in both ensembles, with, if anything, a larger temperature and Atlantic jet response in the AMOC collapsed SSP 2-4.5 ensemble members (Fig. 3).

Though the overall responses in the surface temperatures and winds are very similar, there are some important differences worth noting. First, the SSTs in the $3xCO_2$ simulation show much less cooling over the Pacific northern midlatitudes (> 40°N) compared to the SSP 2-4.5 C simulations, which likely reflects differences in the length of these integrations as this cooling takes centuries to equilibrate (Appendix Figure 1). Second, in response to 3xCO_2 there is much more warming over the NH subtropics and tropics, a feature which reflects the higher CO_2 forcing in that simulation. Thus, in contrast to what occurs in the SSP 2-4.5 C ensemble members, there is no suggestion of SH polar amplification occurring at 3xCO_2.

The differences in SST gradients over the northern high latitude Pacific and tropics and SH occurring in response to 3xCO_2 have implications for the jet and precipitation responses in these regions. In particular, over the Pacific northern midlatitudes, where there is much less cooling than what occurs in the SSP 2-4.5 C integrations, the jet response resembles more of a poleward shift, characterized not only by an acceleration north of 40°N, but also reduced winds ∼ 20°N; in the tropical Pacific there is also a much stronger increase in precipitation, relative to the AMOC SSP 2-4.5 C ensemble.

Even over the North Atlantic the SST cooling is slightly weaker and less expansive and the jet response at 850 hPa is not statistically significant at 3xCO_2, relative to the SSP 2-4.5 collapsed ensemble members. In the SH, there is a weak, albeit not statistically significant, suggestion of a poleward shift of the midlatitude jet at 3xCO_2, which is not evident in the SSP 2-4.5 C integrations. As indicated earlier, all of these differences likely reflect differences in the timescales of the integrations. Nonetheless, despite these subtle differences, the overall similarities between Figures 3 and 6 suggest that the climate response captured moving from 2xCO_2 to 3xCO_2 is, to first order, determined by the changes in AMOC strength occuring in these simulations.

A high degree of consistency is also featured in the vertical response of the large-scale circulation between the AMOC SSP 2-4.5 collapsed ensemble (Fig. 4) and the 3xCO_2 integration (Fig. 7). That is, in concert with stronger cooling over the Arctic (Fig. 7a), the 3xCO_2 simulation features a stronger poleward shift of the NH zonal mean jet (Fig. 7b), increased EKE northward of 40°N (Fig. 7c) and a strengthened Hadley Cell (Fig. 7d).

As near the surface, there are also important differences worth noting in vertical structure. Most noticeably, the amplitude of cooling over the Arctic is much weaker in the 3xCO_2 simulation (Fig. 7a) relative to the collapsed SSP 2-4.5 ensemble (Fig. 4a), reflecting the higher CO_2 forcing moving from 2xCO_2 to 3xCO_2. This is also reflected in the stronger warming occurring within the tropics and southern latitudes. Nonetheless, these differences in absolute temperature occurring

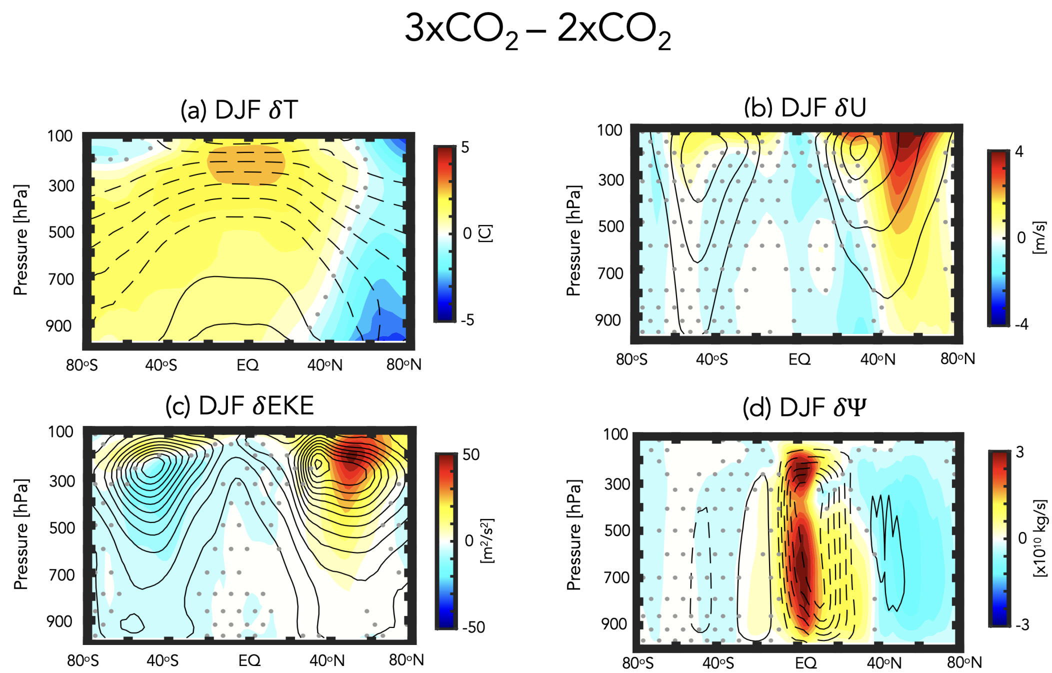

FIG. 7. Same as Figure 4, except showing the difference between the year 120-150 climatological mean $3xCO_2$ and $2xCO_2$ responses.

over the tropics and polar region conspire to produce a similar increase in meridional temperature gradients, compared to the changes in gradients featured in the comparison between the SSP 2-4.5 R and C ensembles. As such, the zonal mean NH jet response is quite similar in the $3xCO_2$ simulation (Fig. 7b) compared to SSP 2-4.5 C (Fig. 4b) and is also coupled to a increase of EKE on the poleward flank of the jet (Fig. 7c). Maps of the EKE response show that at $3xCO_2$ much of this increased EKE reflects changes over the Atlantic (Fig. 5b), as in the SSP 2-4.5 C ensemble (Fig. 5a), although there is also increased EKE over the western Pacific and North America.

To summarize: In response to a collapse of the AMOC, our results show widespread cooling over the Arctic and stronger meridional temperature gradients over the NH. This increase in temperature gradients is associated with a poleward shift of the midlatitude jet (and associated eddy energy) as well as a strengthening of the NH Hadley Cell. In the lower troposphere (> 600 hPa) the NH Hadley cell is displaced poleward.

Over the Northern Hemisphere the response to an increase from $2xCO_2$ to $3xCO_2$ is remarkably similar to the differences between the SSP 2-4.5 R and C simulations, both in terms of the magnitude and spatial pattern of these changes. Some exceptions, however, include the near surface (850 hPa) wind response over the North Atlantic, which is not statisically significant at 3xCO_2, as well as in the tropics, where precipitation increases strongly over the Pacific. There is also more warming in the tropical upper troposphere and SH in the 3xCO_2 simulation. Overall, this close correspondence suggests that the collapse of the AMOC is the dominant driver of the large-scale circulation changes moving from 2xCO_2 to 3xCO_2 in our model.

b. Scaling of Equilibrated Thermodynamic and Dynamic Responses with Global Mean Surface Temperature (GMST)

One question that is not addressed in the previous section is how changes in the climate response to an AMOC collapse scale with changes in GMST. To this end, here we expand our analysis to include the results of additional (4- and 5xCO_2) FOM abrupt CO_2 runs, as well as the results from the SOM abrupt CO_2 integrations.

1) Global Thermodynamic Changes

Figure 8a shows the annual global mean surface temperature response among all of the simulations, plotted as a function of associated instantaneous radiative forcing (RF), where RF is calculated from the expression 5.35ln (NxCO_2/1xCO_2) (Byrne and Goldblatt (2014)) and, for each run, N is the CO_2 multiple of the PI value (2.4, for the case of the SSP 2-4.5 ensemble members). The changes in GMST across this broader range of CO_2 forcing show the nonlinear behavior between the 2- and 3xCO_2 FOM simulations (blue circles) that was first identified in Mitevski et al. (2021) (see their Figure 1). By comparison, the results from the SOM experiments (aqua circles) show no evidence of a nonlinearity. This result was also documented in Mitevski et al. (2021) and suggests that the changes in ocean horizontal and vertical heat fluxes not included in the q-flux experiments are primarily responsible for the nonlinear changes in GMST occurring in the FOM experiments.

Building on Mitevski et al. (2021), here we also include the results from the SSP 2-4.5 R and C ensemble members (red circles, cyan and blue outlines) which are seen to align respectively with the SOM (solid cyan) and FOM (solid blue) scalings. This suggests that the ocean heat convergence changes that occur in the collapsed SSP 2-4.5 C members are primarily responsible for the GMST

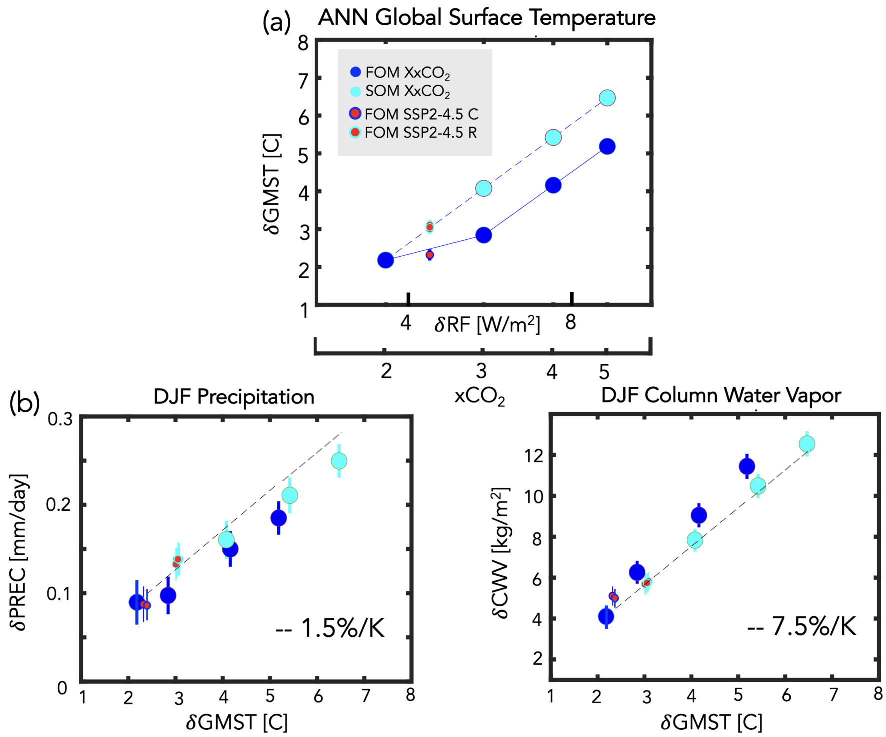

FIG. 8. Top: Changes in annual mean global mean surface temperature (GMST), plotted as a function of the associated radiative forcing (RF), calculated from the expression 5.35ln ($NxCO_2/1xCO_2$) (Byrne and Goldblatt (2014)) where, for each run, N is the CO_2 multiple of the PI value (2.4, for the case of the SSP 2.45 ensemble members), consistent with the presentation in Mitevski et al. (2021). Bottom: Changes in DJF global mean precipitation (left) and atmospheric column water vapor (right). Changes in precipitation and column water vapor are plotted relative to the annual mean GMST changes in (a). Results from the abrupt 2-5xCO_2 fully coupled atmosphere-ocean model (FOM) and slab ocean model (SOM) results are shown in the blue and cyan filled circles. The FOM SSP 2-4.5 recovered (R) and collapsed (C) results are also shown in the red circles (cyan and blue outlines, respectively). Interannual variability for each metric is indicated by the vertical bars. Note that in all panels the SOM 2xCO_2 results have been adjusted to match the FOM 2xCO_2 results in order to facilitate comparison of the FOM and SOM scalings with CO_2 and GMST, not on the absolute magnitude of the responses.

differences, compared to the recovered SSP 2-4.5 R members. Note that the SSP 2-4.5 results are plotted with respect to the peak CO_2 level achieved (i.e. 643 ppm), which occurs at year 2200 (not at the values occurring during years 2400-2500, which are lower (579-598 ppm)) (Meinshausen et al. (2020)).

Next we examine how changes in first-order thermodynamic variables scale with these (nonlinear) changes in GMST. Like the changes in GMST, the changes in global mean precipitation and integrated column water vapor (CWV) also show evidence of a nonlinear behavior, with respect to radiative forcing, occurring in the FOM simulations moving from 2- to 3xCO_2 (Appendix Figure 2). As expected from the GMST changes, this behavior is absent in the SOM integrations and the SSP 2-4.5 C and R members again align with the FOM and SOM scalings, respectively.

However, plotting the precipitation and CWV DJF changes relative to annual mean GMST, reveals that the nonlinear scaling with RF more-or-less disappears (Fig. 8b). This demonstrates that, while the first order global scale hydrological cycle is sensitive to the collapse of the AMOC, this sensitivity occurs primarily through changes in GMST. It is also interesting to note that the lower precipitation values occurring in the SOM integrations, for a given values of GMST, is consistent with the direct effect of greenhouse gases, which tend to suppress global mean precipitation (Samset et al. (2016)).

Finally, we note that the scaling of precipitation and CWV with GMST roughly follow the predictions from Held and Soden (2006), who identified a Clausius-Clapeyron (CC) scaling of integrated column water vapor (dashed black line denoting 7.5%/K, Fig. 8b, left) and a significantly sub-CC scaling of global mean precipitation (1.5%/K, Fig. 8b, right). While some additional nonlinearity in precipitation is also evident at higher CO_2 levels, as this is not immediately relevant to the SSP 2-4.5 ensemble, we reserve further discussion for future work.

2) Northern Hemisphere Dynamical Changes: A Regime Shift

Moving next to the dynamical response, we find that several measures of the NH DJF zonal mean dynamical circulation behave nonlinearly (and even non-monotonically) with respect to radiative forcing in the FOM simulations (Appendix Figure 3). Unlike precipitation and CWV, however, this non-linear behavior in the NH surface wind-based Hadley cell edge (Fig. 8a), Hadley Cell strength (Fig. 8b), northern midlatitude EKE (Fig. 8c), latitude of maximum eddy momentum fluxes (Fig. 8d) and northern midlatitude static stability (Fig. 8e) also occurs after plotting as a function of GMST. Overall, these results suggest that there is no clear (certainly not linear) relationship between the northern Hadley Cell (strength and lower tropospheric edge) and midlatitude jet behavior with GMST in simulations (3xCO_2 and SSP 2-4.5 C) in which the AMOC collapses.

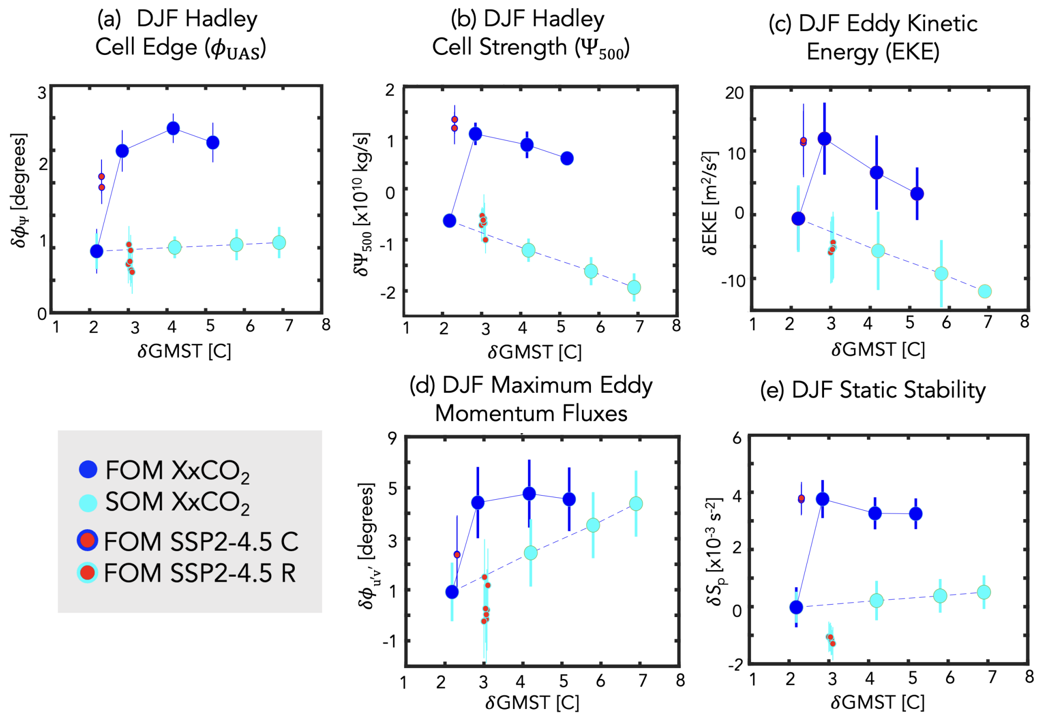

FIG. 9. Changes in various DJF Northern Hemisphere (NH) dynamical metrics, plotted as a function of GMST. Specifically, shown are the Hadley Cell edge (ϕ) (a), Hadley Cell strength (Ψ_{500}) (b), NH column eddy kinetic energy (EKE) (c), latitude of the maximum NH eddy momentum fluxes (d) and NH midlatitude dry static stability (e). The quantities in (a), (b) and (d) are defined in Section 2, while the zonally averaged EKE and static stability changes have both been averaged over 300-1000 hPa and 30°N-60°N. Results from the abrupt 2-5xCO_2 fully coupled atmosphere-ocean model (FOM) and slab ocean model (SOM) results are shown in the blue and cyan filled circles. The FOM SSP 2-4.5 recovered (R) and collapsed (C) ensemble members are shown in the red circles (cyan and blue outlines, respectively). Interannual variability for each metric is indicated by the vertical bars. As in Figure 8 the SOM 2xCO_2 results have been adjusted to match the FOM 2xCO_2 results.

Rather, the changes in both the NH Hadley Cell edge and strength reflect an abrupt poleward shift and increase, respectively, moving from 2- to 3xCO_2 and between the SSP 2-4.5 R and SSP 2-4.5 C ensemble members. This abrupt poleward shift and strengthening saturates at 3xCO_2 and even decreases at higher CO_2 values for certain metrics, despite continued increases in GMST (Fig. 9b, 9c). As such, this saturation in the NH circulation is indicative of a "regime" shift in our model, consistent with the use of the term in Caballero and Langen (2005), albeit for the low-gradient, high temperature regime identified in their study using a more idealized model (see discussion in

Section 4). In particular, our results suggest that the AMOC collapse is associated with a regime shift in our model between a climate state in which the Hadley Cell is substantially weaker and displaced equatorward (strong AMOC) and a state in which the Hadley Cell and midlatitude EKE is stronger and displaced poleward (weak AMOC).

Note that, while the increases in Hadley Cell strength (Fig. 9b) have been well documented, the poleward shift in the northern Hadley Cell edge has been less examined (Fig. 9a). Our examination of the Hadley Cell edge, as gauged using the surface zonal winds, is partly motivated by the results presented in Figure 3b, which show increased SLP over the North Pacific and Atlantic high latitudes. That is, the SLP increases over the North Atlantic extend as far south as 40°N and thus, together with the Pacific response, reflect a pattern which is consistent with the SLP pressure signature of an expanded northern edge of the Hadley cell (Schmidt and Grise (2017)). Another motivation comes from KB2021, who suggest that, in addition to reduced warming over the Arctic, stronger tropical heating and a related expansion of the HC may contribute to the poleward shift of the northern jet, although this was never explicitly shown.

The fact that changes in the Hadley Cell and midlatitude eddy-driven jet are linked is consistent with recent studies showing that the HC edge is strongly linked to the latitude of maximum eddy momentum fluxes, such that a poleward shift of the jet is associated with HC expansion (Chemke and Polvani (2019), Waugh et al. (2018), Menzel et al. (2019)). As discussed in those studies, this connection is likely associated with changes in the latitude of the maximum eddy momentum fluxes and the vertical potential temperature gradient (i.e., the static stability, $S_p = -(\frac{T}{\Theta})(\frac{\partial \Theta}{\partial P})$) over northern midlatitudes, which also exhibit regime shifts in the NH (Fig. 9 d-e). The sensitivity of the extratropical tropospheric eddy response to even modest changes in isentropic slope, resulting both from changes in baroclinicity and static stability, is well known (Thompson and Birner (2012)) and previous studies have shown that increases in static stability can increase subtropical baroclinicity, causing the HC edge and subtropical eddy fields to shift poleward (Chemke and Polvani (2019); Menzel et al. (2019)). Note that the changes in EKE and static stability are shown averaged over 300-1000 hPa and over 30°N-60°N; similar results are found averaging over the entire hemisphere poleward of 20°N.

Another interesting feature highlighted in Figure 9 is that for some variables even the *sign* of the response is different than would otherwise be predicted from the SOM experiments which ignore

AMOC-associated changes in ocean heat convergence. This applies both to the changes in Hadley Cell strength (Fig. 9b) and tropospheric column averaged EKE (Fig. 9c) which otherwise decrease in response to increasing CO_2. This role of the ocean in the behavior of projected changes in northern EKE is consistent with Chemke et al. (2022), who showed that changes in ocean heat convergence are essential for correctly capturing the sign of the projected response in future storm track changes over the North Atlantic.

To further relate the changes in the Hadley Cell to the changes in midlatitude eddies, Figure 10 shows the evolution of the response in northern HC strength, EKE, baroclinic eddy generation, and midlatitude static stability. Consistent with increases in dry static stability in the $3xCO_2$ and SSP 2-4.5 simulations, there is an increase in the generation of northern midlatitude tropospheric baroclinic eddies and eddy kinetic energy and an intensification of the northern HC. The similar behavior among all variables suggests that they are mechanistically related. Furthermore, while changes in tropopause height have also been invoked to interpret future changes in the midlatitude jet stream (Cronin and Jansen (2016), Held (1993), Vallis et al. (2015)) and edge of the Hadley Cell (Lu et al. (2007)), we do not observe a consistent response in tropopause height between the $3xCO_2$ and SSP 2-4.5 C integrations (not shown), suggesting that tropopause height changes alone are not the primary drivers of the Hadley Cell and jet behaviors exhibited in these runs.

Note that the close relationship between the changes in HC strength and midlatitude eddies suggested in Figure 10 initially appears at odds with the findings in Menzel et al. (2019), who showed a strong disconnect between the strength of the subtropical jet and the edge of the Hadley Cell. However, that study inferred this disconnect based on interannual variability and the response to an abrupt $4xCO_2$ forcing, which both yield a weakening and poleward shift of the Hadley Cell. By comparison, in connection with a southward shifted ITCZ a collapse of the AMOC is associated with a strengthened Hadley Cell (Zhang and Delworth (2005); Orihuela-Pinto et al. (2022)).

c. Energetic Analysis: Bjerknes Compensation in Response to an AMOC Shutdown

The previous section showed that, unlike the global mean thermodynamic response, several measures of NH dynamical sensitivity do not scale linearly with changes in global mean surface temperature. Rather, a collapsed AMOC in our model is accompanied by an abrupt strengthening and northward shift of the Hadley Cell and northern midlatitude jet. To better understand why these

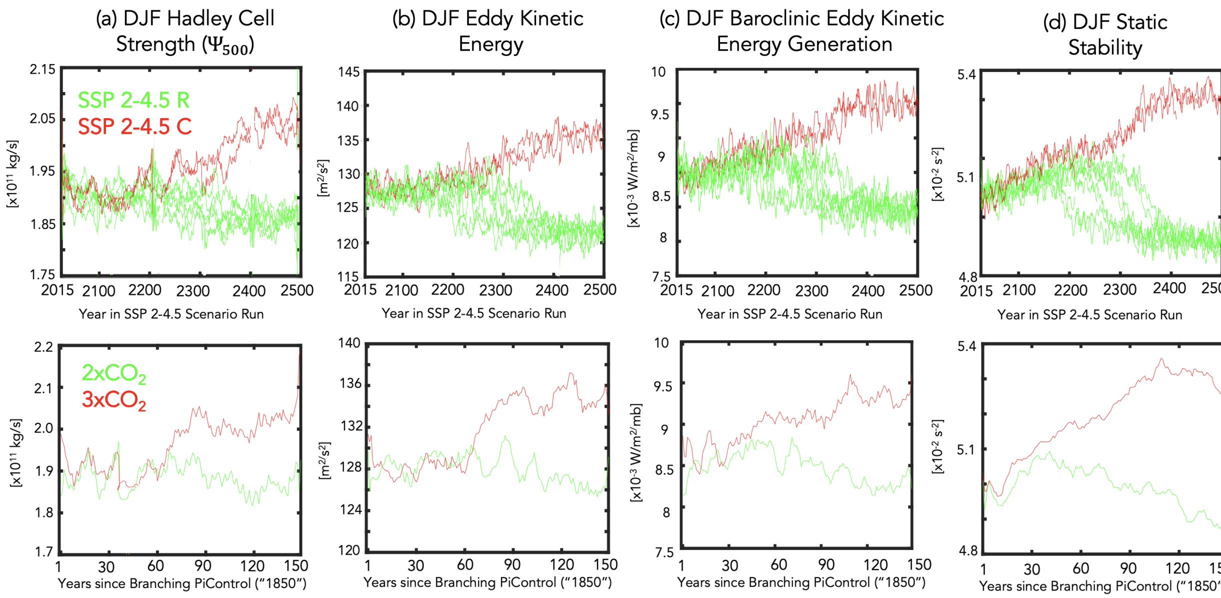

FIG. 10. Evolution of DJF Northern Hemisphere Hadley Cell strength (a), eddy kinetic energy (b), baroclinic eddy kinetic energy generation (c) and midlatitude dry static stability (d). The baroclinic eddy generation has been averaged over the same region (300-1000 hPa, 30°N-60°N) as the EKE and static stability fields, consistent with Figure 9. Comparisons among the SSP 2-4.5 recovered (R) and collapsed (C) ensemble members (top panels) and between the 2- and $3xCO_2$ runs (bottom panels) are shown in the green and red lines, respectively. A 5-year moving average has been applied to all time series.

variables exhibit this regime shift we examine the changes in energetics – and their partitioning between the atmosphere and ocean – that arise moving from 2- to $3xCO_2$ and between the SSP 2-4.5 R and SSP 2-4.5 C members.

1) Ocean and Atmosphere Compensation

Figure 11 shows the response in the annual mean northward total (atmosphere + ocean), oceanic and atmospheric transports, relative to the preindustrial control simulation. Between $2xCO_2$ and $3xCO_2$ and between the SSP 2-4.5 R and SSP 2-4.5 C members there is a large decrease/increase in T_O/T_A over northern latitudes with a peak located at ~30-40°N. This behavior is reflective of an abrupt Bjerknes compensation that emerges in the model, wherein large anomalies in heat transported by the atmosphere increase to approximately balance large reductions in northward ocean transport (Bjerknes (1964)). More precisely, the reduction in northward ocean heat transport

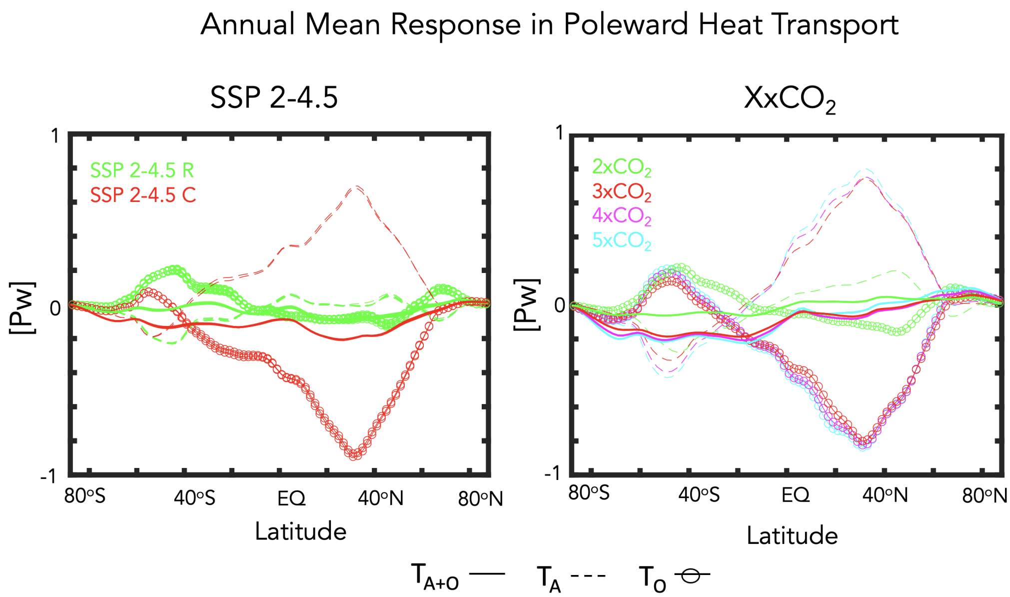

FIG. 11. Changes in the annual mean atmospheric (T_A), oceanic (T_O) and total (atmospheric + oceanic, T_{A+O}) northward energy transport, relative to the preindustrial control simulation. Results from the SSP 2-4.5 ensemble members and the 2-5xCO_2 simulations are shown in the left and right panels. The simulations in which the AMOC collapses (3xCO_2, SSP 2-4.5 C) versus recovers (2xCO_2, SSP 2-4.5 R) are highlighted in the red and green lines, respectively.

in the SSP 2-4.5 C ensemble members and at 3xCO_2 is approximately 1 PW (Fig. 11), representing a ~ 50% decrease relative to preindustrial values (Fig. 2b). Magnusdottir and Saravannan (1999) attributed this compensatory response in the atmosphere to high dynamical efficiency of atmospheric eddy transport. Note that the annual mean is shown here to facilitate comparison with the annual mean results presented in previous studies (e.g., see Figure 1 in Zhang and Delworth (2005) and Figure 5 in Zhang et al. (2010)). We note in passing that the responses in the boreal winter transports look very similar (not shown).

What Figure 11 makes clear is that the changes in ocean heat transport are dominated by the changes in the AMOC, as reflected in the magnitude of the compensation occurring at 3xCO_2 (similar to the compensation occurring in the SSP 2-4.5 C ensemble) which saturates, despite further increases in CO_2 (and GMST). This helps to explain the behavior of the dynamical indices discussed in the previous section (Fig. 9), which also saturate at 3xCO_2 and do not increase (rather, decrease) moving to higher CO_2 forcings. A dramatic reduction in poleward ocean heat transport at ~30-40°N was also noted in the CMIP5 historical models in association with strong air-sea interactions within the midlatitude storm tracks (Outten et al. (2018)) and in several future climate integrations performed using the CMIP5 version of the GISS climate model (E2) Rind et al. (2018). In the latter case, however, the near cessation of the AMOC severely limited, but did not entirely shut off, poleward heat transport, which was partly maintained through the ocean subtropical gyre contribution. Our results also show stronger compensation occurring over SH high latitudes poleward of 40°S.

While the changes in T_O and T_A reflect near entire compensation, this compensation is nonetheless not perfect and slightly negative, resulting in a net reduction in the total northward combined atmospheric and oceanic energy transport. This reduction in net poleward energy transport was also found in Liu et al. (2020), who showed that a weakened AMOC caused a larger energy change at the Earth's surface than at the TOA (their Figure S.5). In particular, over the NAWH region they found that more energy was taken from the atmosphere through surface turbulent heat fluxes, resulting in a situation where the NH atmosphere loses more energy at the surface compared to the energy that is gained at the TOA (through reduced OLR). In the GISS model we also find that there is more energy loss at the surface compared to changes at the TOA and that these are primarily associated with reduced latent heat fluxes (Appendix Figure 4). The reductions in surface latent heat fluxes occur over the North Atlantic and are strongly shaped by changes in evaporation (not shown). The exact extent and nature of this compensation, however, is likely shaped strongly by cloud feedbacks (Zhang et al. (2010)) as discussed more in Section 4b.

2) Moist vs. Dry Atmospheric Transports

To better understand the nature of the compensation occurring in the GISS model, Figure 12 further decomposes the changes in T_A into changes in the northward transports of latent heat (Fig. 12a) and dry static energy (Fig. 12b). Over the SH the changes in dry and moist static energy nearly compensate in all simulations, resulting in weakly negative northward atmospheric transports poleward of ~40°S in both the $XxCO_2$ and SSP 2-4.5 runs. Equatorward of ~40°S, however, this behavior transitions in the SSP 2-4.5 C members to net positive northward atmospheric transport from the SH subtropics towards and across the equator (which compensates the reduction in oceanic equatorward heat transport in that region evident in Figure 11). This behavior over the SH

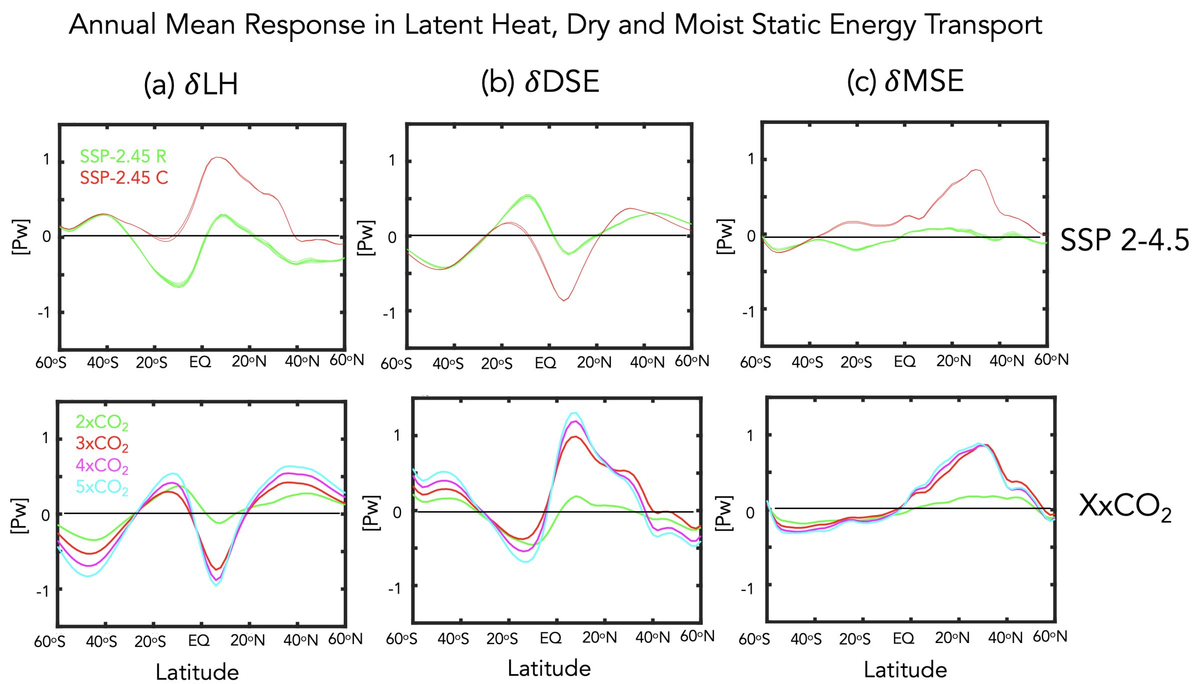

FIG. 12. Changes in the annual mean atmospheric latent heat (a), dry static energy (b) and total moist static energy (c) northward transports, relative to the preindustrial control simulation. Results from the SSP 2-4.5 ensemble members and the 2-5xCO_2 simulations are shown in the top and bottom panels. The simulations in which the AMOC collapses (3xCO_2, SSP 2-4.5 C) versus recovers (2xCO_2, SSP 2-4.5 R) are highlighted in the red and green lines, respectively.

subtropics is distinct from what occurs in the XxCO_2 simulations, in which there is overall reduced northward atmospheric transport (and less compensation by the oceanic transports). The fact that the oceanic compensation in this region is weaker at 3xCO_2 (relative to the SSP 2-4.5 C members) may reflect the differences in simulation length between the abrupt CO_2 and SSP 2-4.5 integrations or the fact that at 3xCO_2 there is increased water vapor in the atmosphere in the warmer climate and hence increased poleward latent heat transport. Notably, however, the AMOC response in all runs has little effect on extratropical latent heat transport over the Southern Hemisphere extratropics.

Aside from the subtle differences between the 3xCO_2 and SSP 2-4.5 C runs that occur over the SH subtropics, the fact that the changes in dry static energy (DSE) and latent heat transport nearly compensate over southern and tropical latitudes in all runs is consistent with the expectation from Held and Soden (2006). Interestingly, however, this compensation does not occur over northern latitudes spanning ~10^{o}N to ~40^{o}N, resulting in a net increase in poleward moist static energy transport (Fig. 12c). Over these latitudes the increased atmospheric energy transport resulting from an AMOC collapse is almost entirely due to changes in dry static energy, not latent heat transport. In particular, DSE transport exhibits a "jump" between 2xCO_2 and 3xCO_2 (also evident in the differences between the SSP 2-4.5 C and SSP 2-4.5 R members) (Fig. 12b); a similar jump is only evident in the latent heat transports equatorward of 20^{o}N (and, if anything, enhances energy transport equatorward, not poleward). The jump in DSE transport over the northern extratropics saturates for forcings greater than 3xCO_2. Further analysis of the evolution of the dry static energy transports at different latitudes in the northern hemisphere (not shown) reveals that these changes in DSE transport first emerge between 30^{o}N-40^{o}N and propagate thereafter to higher latitudes.

The fact that the abrupt increase in atmospheric poleward transport derives primarily from changes in DSE transport helps in interpreting why a similar shift emerges in the Hadley Cell and eddy-driven jet, since the Hadley cell fluxes dry static energy poleward (Frierson et al. (2007)). Indeed, previous energetic definitions of the storm track have appealed directly to DSE (e.g. latitude of maximum vertically-integrated dry static energy flux (Hoskins and Valdes (1990)). More recently, Lachmy and Shaw (2018) show that the vertically integrated eddy potential energy flux shifts in same sense as the vertically integrated eddy DSE flux. They then use the Eliassen-Palm flux relation to connect these changes in energy fluxes to changes in the eddy momentum fluxes. Therefore, the fact that these features all shift in concert with each other in our runs should perhaps not be too surprising.

4. Discussion

a. Caveats Concerning Model Biases

One important caveat with our results relates to known biases in vertical mixing in the ocean component of the GISS model, as discussed in Miller et al. (2021). This biased mixing is likely related to why E2.1 exhibits a more sensitive AMOC response to a quadrupling of CO_2, compared to some other CMIP6 models (KB2021). In addition, Rind et al. (2020) showed that the parameterization of rainfall evaporation associated with moist convective precipitation has a strong influence on the AMOC sensitivity to greenhouse gas forcing in the E2.1 (and higher top E2.2) models, likely via its effect on moisture loading in the atmosphere. Thus, in addition to oceanic processes, atmospheric parameterizations could also be influencing this result.

Along with biases in vertical mixing, the ocean component of E2.1 is also low resolution (one degree). This likely has direct implications for the stability of the AMOC, as discussed in AR2022 (see references therein). In particular, the stability of the AMOC will differ between low resolution climate models, which exhibit a negative salt-advection feedback (leading to salinification of the subpolar gyre and AMOC recovery), and eddy-permitting models, which tend to exhibit a stable AMOC-off state. We emphasize here, however, that throughout we have focused on the response of the atmospheric circulation given a collapse in the AMOC. Thus, while the particular mechanisms by which the AMOC is weakened (and subsequently recovers) in E2.1 may be model-specific, our focus has been on quantifying the atmospheric changes. We also note that Mitevski et al. (2021) showed that the behavior of the AMOC in E2.1 was similar to the response in CESM-LE; furthermore that model also featured a nonlinear response in GMST related to a collapse of the AMOC, albeit one occurring at the transition between 3- and $4xCO_2$.

b. Bjerknes Compensation: Cloud Feedbacks and Dry Versus Moist Energy Transports

A key result from our study is that a collapse of the AMOC results in a regime shift in various components of the NH large-scale circulation and this shift is reflective of an abrupt Bjerknes compensation that emerges at $3xCO_2$ and in the SSP 2-4.5 C ensemble members. There are several aspects of this compensation, however, that require closer examination. Among others, these include:

1) Influence of Cloud Feedbacks

Mitevski et al. (2022) showed that nonlinearity in ECS occurring between 2- and $3xCO_2$ in our model was related to nonlinear variations in the atmospheric feedback parameter and not to changes in radiative forcing. At the same time, the strength of the Bjerknes compensation in our model will likely depend on cloud feedbacks, as the right-hand-side of Equation (1) makes clear (via the F_T and F_S terms). For example, Zhang et al. (2010) showed a strong sensitivity of the tropical climates' response to to changes in cloud feedbacks, showing that in a model with no cloud feedbacks the tropical response to the weakening of the AMOC (including its southward ITCZ shift) was much smaller. Thus, while the overall Bjerknes compensation occurring in our model is generally consistent (in its meridional distribution and amplitude) with the results from other similar studies, the exact details of how compensation occurs is likely to be sensitive to local climate feedbacks which may be model-dependent and/or poorly constrained by observations. Future work will focus on better understanding how changes in cloud feedbacks modulate the response of the atmosphere to a weakened AMOC in our model.

2) Atmospheric Dry vs. Moist Compensation

One interesting result from this study is that the large compensation in poleward atmospheric transport that occurs as the AMOC collapses is primarily related to increases in the northward transport of dry static energy northward of 20°N (coincident with the edge of the non-monotonically shifting HC edge) (Fig. 12). This result is initially surprising as it downplays the compensation that occurs through changes in latent heat transport over northern midlatitudes. Thus, while our results do show a compensatory latent heat transport occurring in the tropics, this does not occur over the NH extratropics and is therefore not fundamentally associated with the non-monotonic behavior in the NH Hadley Cell edge and midlatitude eddy-driven jet.

The diminished importance of the latent heat transports over northern midlatitudes is initially surprising, given that warming in response to increased CO_2 results in an overall increase in atmospheric water vapor. Upon further reflection, however, this effect of enhanced global warming needs to be considered in the context of both the reduced Arctic warming and poleward shifted EKE evident in Figure 4. The former can, via cooling, reduce the total moisture available for northward transport, while the latter would impact the efficiency with which subtropical moisture is transported poleward to higher latitudes. In our results it appears that these changes compensate, resulting in no net AMOC imprint on the latent heat transports over northern extratropical latitudes (Fig. 10a, bottom). While disentangling these contributions is beyond the scope of this study, we do comment on the consistent results shown in Figure S5 of Mitevski et al. (2021), who identified a much stronger non-monotonicity present in the edge of the dry zone (P-E) compared to NH specific humidity. While this suggests that the circulation changes are themselves responsible for the behavior of the latent heat transports (and not vice versa), more work is needed to understand the underlying mechanism present in our model and whether this behavior is also exhibited in other models (or the real atmosphere).

5. Conclusions

Here we have documented the atmospheric response to an AMOC collapse using the CMIP6 version of the NASA GISS climate model (E2.1). Using simulations from an identically forced (SSP 2-4.5) ensemble in which the AMOC collapses and recovers in two and eight members, respectively, we have isolated the atmospheric response to a spontaneous collapse of the AMOC in the context of a warming climate, absent any external perturbations that may interfere with the model's internal dynamics. By comparison, previous studies have all needed to employ (negative) freshwater flux perturbations or similar AMOC "locking" methods (Liu et al. (2020), Orihuela-Pinto et al. (2022)). We then placed the atmospheric response in the SSP 2-4.5 simulations in the context of a broad set of integrations in which CO_2 is abruptly increased, run both in fully coupled atmosphere-ocean (FOM) and slab-ocean (SOM) configurations, in which changes in ocean heat flux convergences are respectively included and neglected. Our main results are as follows:

1. In our model a sustained decline and eventual collapse of the AMOC results in a strengthening of the NH Hadley cell and the northern midlatitude jet as well as an abrupt northward shift of the Hadley Cell edge in the lower troposphere. Quite remarkably, these features dominate the large-scale atmospheric circulation response that occurs in the NH moving from $2xCO_2$ to $3xCO_2$.

2. For certain variables (i.e., HC strength, EKE) an ultimate collapse of the AMOC produces changes that are *opposite* in sign to the response to increased CO_2 forcing that occurs in the absence of ocean circulation changes.

3. The regime shift in the NH large-scale circulation reflects an abrupt Bjerknes compensation that emerges in the $3xCO_2$ and collapsed SSP 2-4.5 C simulations. This compensation is located further south (~40^{o}N) than what is often considered to be the main region of maximum ocean-atmosphere compensation (70^{o}N) (Shaffrey and Sutton (2006)) and reflects a key role for the midlatitude storm tracks in the coupled system's response to a warmer climate.

4. The impact of the AMOC on the large-scale NH circulation occurs mainly through its influence on mean free-tropospheric temperature gradients, not GMST. This finding reinforces growing evidence that the climate's "dynamical sensitivity" does not scale with equilibrium climate sensitivity (Grise and Polvani (2016), Ceppi et al. (2018)) , particularly in the presence of a collapsed AMOC .

The regime shift in NH dynamics resulting from an AMOC collapse in our model is, to the best of our knowledge, the first time that such behavior has been documented for a CMIP class model. While previous studies have also reported nonlinear behaviors in Hadley Cell strength (Levine and Schneider (2011), O'Reilly et al. (2016)) these studies have employed mainly idealized models. In addition to the changes in the Hadley Cell we also identify a regime shift in the behavior of the northern storm tracks. This result brings to mind the findings from Caballero and Langen (2005), who showed that poleward energy transport increases over a range of increasing surface temperature but saturates in the low-gradient, high temperature regime. As in our study, they attribute this "low-gradient" paradox to increasing tropospheric static stability and the poleward migration of the storm tracks. However, they too employed a highly idealized (aquaplanet) model and find that this saturation in storm track behavior is related to a saturation of latent heat transport. Our results, by comparison, highlight the role of compensatory dry static energy transports and suggests that studies accounting for dynamic ocean-atmospheric coupling (i.e., changes in vertical and horizontal ocean heat fluxes) may come to different conclusions about the nature of compensation in the atmosphere.

In addition to contributing to improved understanding of the coupled atmosphere-ocean response to a weakening of the AMOC, our results also have a practical implication for the purpose of developing storylines of atmospheric circulation changes (Zappa and Shepherd (2017)) and for interpreting model differences in projected storm tracks. In particular, while the use of "global warming levels" applied throughout the IPCC AR6 report may suffice for understanding the global hydrological cycle (Hausfather et al. (2022)) here we have shown that this does not hold true for projections of the NH jet stream and Hadley Cell edge. This underscores the need to understand the direct impact of the AMOC on meridional temperature gradients and not only on surface temperature.

Finally, preliminary analysis of the high-top GISS climate model (E2.2 (Rind et al. (2020), Orbe et al. (2020)) suggests a different sensitivity of the AMOC compared to E2.1 (occurring between $3xCO_2$ and $4xCO_2$). Understanding these differences and how they are reflected in different Bjerknes compensations will be described in a follow-up paper.

Acknowledgments. C.O. thanks Ivan Mitevski for processing the zonally varying eddy kinetic energy fields that were used as part of this analysis. Climate modeling at GISS is supported by the NASA Modeling, Analysis and Prediction program, and resources supporting this work were provided by the NASA High-End Computing (HEC) Program through the NASA Center for Climate Simulation (NCCS) at Goddard Space Flight Center.

Data availability statement. The CMIP6 SSP 2-4.5 data used in this study is available from the Earth System Grid Federation (ESGF) (https://esgf-node.llnl.gov/search/cmip6/) or from the NASA Center for Climate Simulations (NCCS) (https://portal.nccs.nasa.gov/datashare/giss/cmip6/). The specific simulations used here are a subset of the historical r[1-10]i1p1f2 (doi:87010.22033/ESGF/CMIP6.7127) and SSP 2-4.5 r[1-10]i1p1f2 (doi:10.22033/ESGF/CMIP6.7415) runs. The XxCO_2 data used to produce the figures in the study is publicly available in a Zenodo repository at https://doi.org/10.5281/zenodo.3901624. The authors acknowledge the World Climate Research Programme's Working Group on Coupled Modeling and we thank all climate modeling groups for making available their model output. All GISS ModelE components are open source and available at https://www.giss.nasa.gov/tools/modelE/.

APPENDIX

Appendix Figures

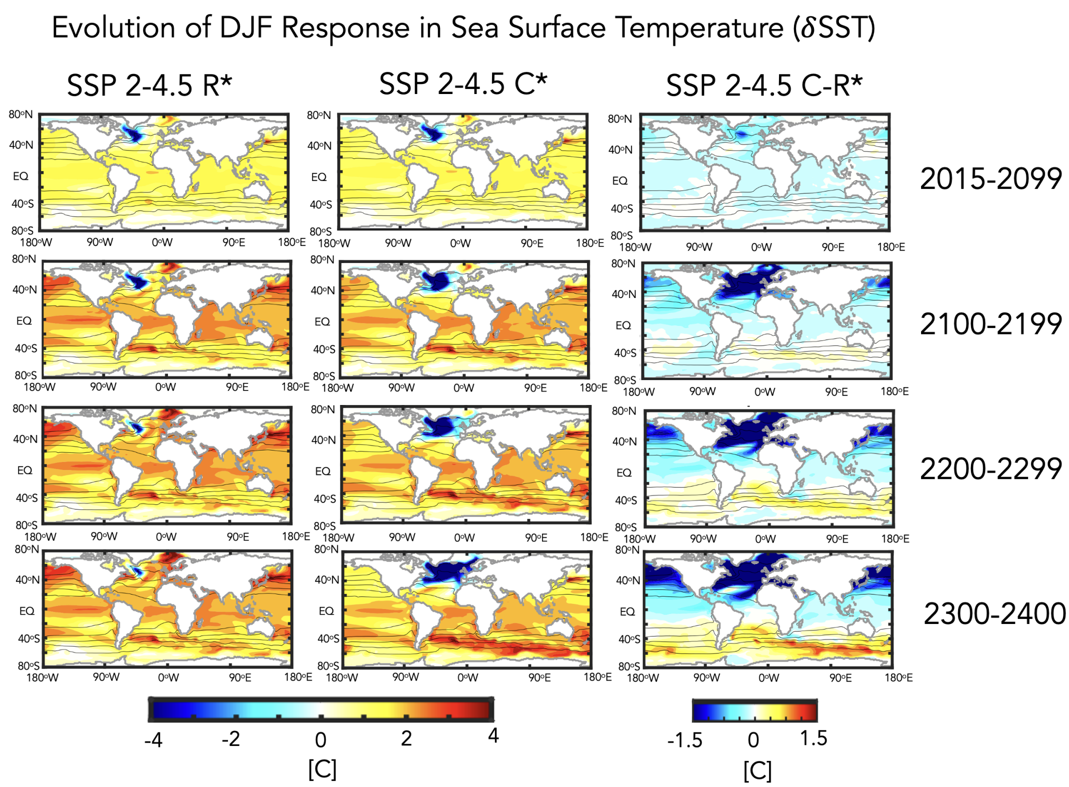

FIG. A1. The evolution of the DJF sea surface temperature difference, relative to the preindustrial control simulation, in one of the SSP 2-4.5 recovered (R) (left) and collapsed (C) ensemble members (middle). The difference between the SSP 2-4.5 recovered and collapsed ensemble members is also shown (right). Note that only one ensemble member is used due to the different recovery times of the AMOC among the "recovered" ensemble members prior to year 2400. Climatological mean values from the preindustrial control simulation are denoted in the black contours.

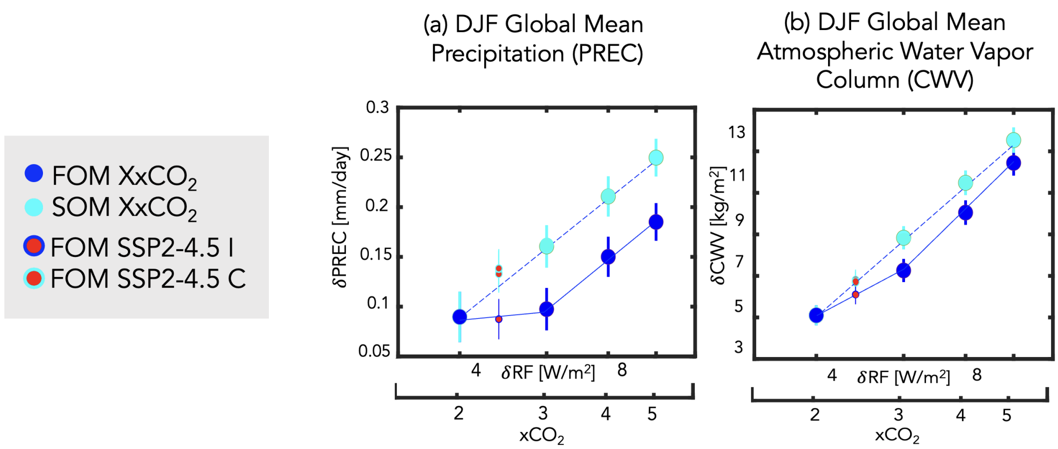

974 FIG. A2. Changes in DJF global mean precipitation (a) and atmospheric column water vapor (b), plotted as a function of the associated radiative forcing (RF), calculated from the expression 5.35ln ($NxCO_2/1xCO_2$) (Byrne Goldblatt (2014)) where, for each run, N is the CO_2 multiple of the PI value (2.4, for the case of the SSP 2-4.5 ensemble members). Results from the abrupt 2-5xCO_2 fully coupled atmosphere-ocean model (FOM) and slab ocean model (SOM) results are shown in the blue and cyan filled circles. The FOM SSP 2-4.5 recovered and collapsed ensemble members are also shown in the red circles (cyan and blue outlines, respectively). Interannual variability for each metric is indicated by the vertical bars.

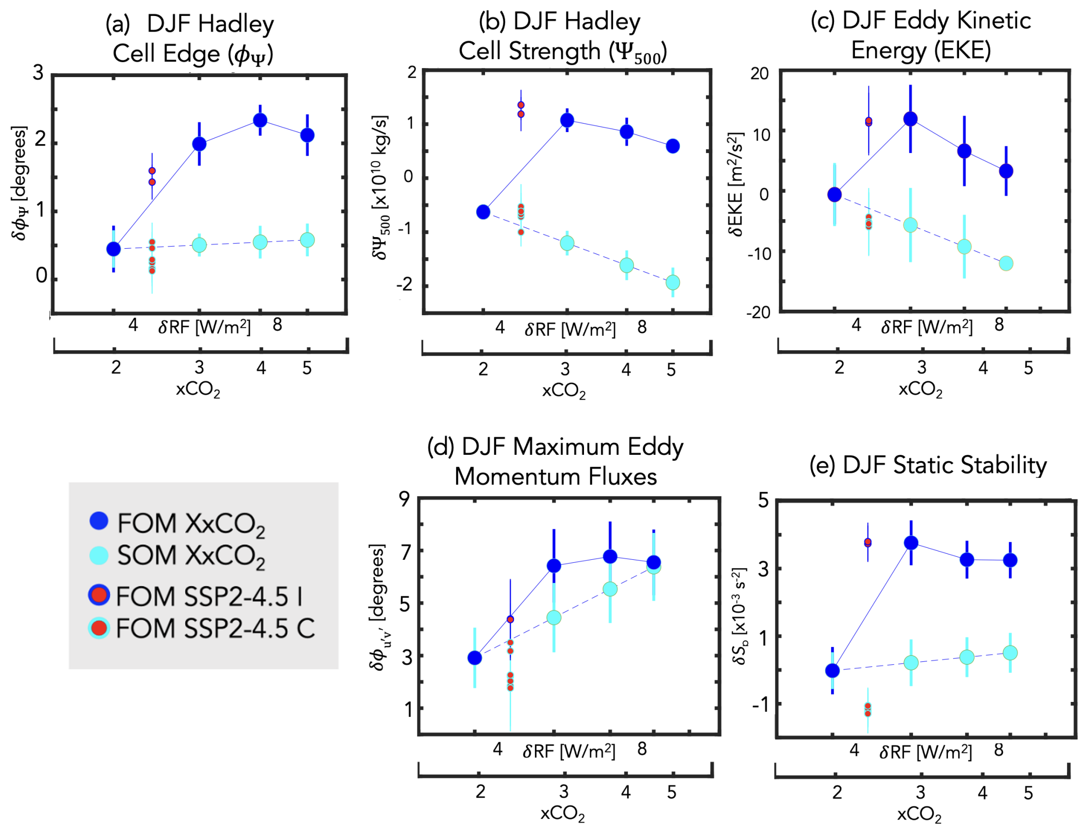

FIG. A3. Changes in various DJF Northern Hemisphere (NH) dynamical metrics, plotted as a function of associated radiative forcing. Specifically, shown are the Hadley Cell edge (ϕ_{UAS}) (a), Hadley Cell strength (Ψ_{500}) (b), NH column eddy kinetic energy (EKE) (c), latitude of the maximum NH eddy momentum fluxes (d) and NH midlatitude dry static stability (e). The quantities in (a), (b) and (d) are defined in Section 2, while the zonally averaged EKE and static stability changes have both been averaged over 300-1000 hPa and 30°N-60°N. Results from the abrupt 2-5xCO_2 fully coupled atmosphere-ocean model (FOM) and slab ocean model (SOM) results are shown in the blue and cyan filled circles. The FOM SSP 2-4.5 recovered and collapsed ensemble members shown in the red circles (cyan and blue outlines, respectively). Interannual variability for each metric is indicated by the vertical bars.

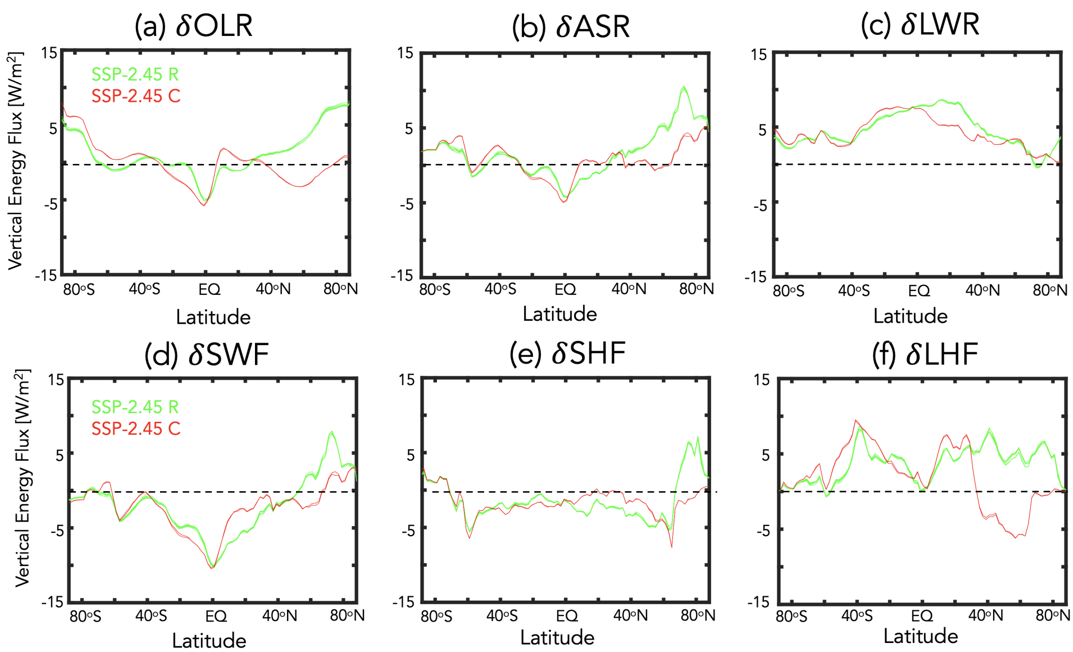

FIG. A4. Changes in the annual mean top of the atmosphere outgoing longwave radiation (OLR) (a) and absorbed shortwave radiation (ASR) (b) and the downward fluxes of radiation at the surface, decomposed into longwave (LWF) (c) and shortwave (SWF) (d) components. The fluxes of latent and sensible heat at the surface (LHF and SHF) are shown in (e) and (f), respectively. All changes are shown for the SSP 2-4.5 collapsed (C) (red) and SSP 2-4.5 recovered (R) (green) ensemble members and are defined relative to the preindustrial control simulation.

References

Adam, O., and Coauthors, 2018: The TropD software package (v1): standardized methods for calculating tropical-width diagnostics. *Geoscientific Model Development*, **11 (10)**, 4339–4357.

Bellomo, K., M. Angeloni, S. Corti, and J. von Hardenberg, 2021: Future climate change shaped by inter-model differences in Atlantic meridional overturning circulation response. *Nature Communications*, **12 (1)**, 1–10.

Bjerknes, J., 1964: Atlantic air-sea interaction. *Advances in geophysics*, Vol. 10, Elsevier, 1–82.

Brayshaw, D. J., T. Woollings, and M. Vellinga, 2009: Tropical and extratropical responses of the north atlantic atmospheric circulation to a sustained weakening of the moc. *Journal of Climate*, **22 (11)**, 3146–3155.

Byrne, B., and C. Goldblatt, 2014: Radiative forcing at high concentrations of well-mixed greenhouse gases. *Geophysical Research Letters*, **41 (1)**, 152–160.

Caballero, R., and P. L. Langen, 2005: The dynamic range of poleward energy transport in an atmospheric general circulation model. *Geophysical Research Letters*, **32 (2)**.

Caesar, L., S. Rahmstorf, A. Robinson, G. Feulner, and V. Saba, 2018: Observed fingerprint of a weakening Atlantic ocean overturning circulation. *Nature*, **556 (7700)**, 191–196.

Ceppi, P., G. Zappa, T. G. Shepherd, and J. M. Gregory, 2018: Fast and slow components of the extratropical atmospheric circulation response to CO_2 forcing. *Journal of Climate*, **31 (3)**, 1091–1105.

Chemke, R., and L. M. Polvani, 2019: Exploiting the abrupt 4× CO_2 scenario to elucidate tropical expansion mechanisms. *Journal of Climate*, **32 (3)**, 859–875.

Chemke, R., L. Zanna, C. Orbe, L. T. Sentman, and L. M. Polvani, 2022: The future intensification of the North Atlantic winter storm track: the key role of dynamic ocean coupling. *Journal of Climate*, **35 (8)**, 2407–2421.

Cheng, W., J. C. Chiang, and D. Zhang, 2013: Atlantic meridional overturning circulation (AMOC) in CMIP5 models: RCP and historical simulations. *Journal of Climate*, **26 (18)**, 7187–7197.

Cronin, T. W., and M. F. Jansen, 2016: Analytic radiative-advective equilibrium as a model for high-latitude climate. *Geophysical Research Letters*, **43 (1)**, 449–457.

Deser, C., and A. S. Phillips, 2009: Atmospheric circulation trends, 1950–2000: The relative roles of sea surface temperature forcing and direct atmospheric radiative forcing. *Journal of Climate*, **22 (2)**, 396–413.

Drijfhout, S., G. J. Van Oldenborgh, and A. Cimatoribus, 2012: Is a decline of AMOC causing the warming hole above the North Atlantic in observed and modeled warming patterns? *Journal of Climate*, **25 (24)**, 8373–8379.

Frierson, D. M., I. M. Held, and P. Zurita-Gotor, 2007: A gray-radiation aquaplanet moist GCM. Part II: Energy transports in altered climates. *Journal of the Atmospheric Sciences*, **64 (5)**, 1680–1693.

Gervais, M., J. Shaman, and Y. Kushnir, 2019: Impacts of the North Atlantic warming hole in future climate projections: Mean atmospheric circulation and the North Atlantic jet. *Journal of Climate*, **32 (10)**, 2673–2689.

Grise, K. M., and L. M. Polvani, 2014: The response of midlatitude jets to increased co2: Distinguishing the roles of sea surface temperature and direct radiative forcing. *Geophysical Research Letters*, **41 (19)**, 6863–6871.

Grise, K. M., and L. M. Polvani, 2016: Is climate sensitivity related to dynamical sensitivity? *Journal of Geophysical Research: Atmospheres*, **121 (10)**, 5159–5176.

Grise, K. M., and L. M. Polvani, 2017: Understanding the time scales of the tropospheric circulation response to abrupt co2 forcing in the southern hemisphere: Seasonality and the role of the stratosphere. *Journal of Climate*, **30 (21)**, 8497–8515.

Haarsma, R., F. Selten, and S. Drijfhout, 2015: Decelerating Atlantic meridional overturning circulation main cause of future west european summer circulation changes. *Environmental Research Letters*, **10 (9)**.

Hausfather, Z., K. Marvel, G. A. Schmidt, J. W. Nielsen-Gammon, and M. Zelinka, 2022: Climate simulations: Recognize the ‘hot model’problem. Nature Publishing Group.

Held, I. M., 1993: Large-scale dynamics and global warming. *Bulletin of the American Meteorological Society*, **74 (2)**, 228–242.

Held, I. M., and B. J. Soden, 2006: Robust responses of the hydrological cycle to global warming. *Journal of climate*, **19 (21)**, 5686–5699.

Hoskins, B. J., and P. J. Valdes, 1990: On the existence of storm-tracks. *Journal of Atmospheric Sciences*, **47 (15)**, 1854–1864.

Jackson, L., R. Kahana, T. Graham, M. Ringer, T. Woollings, J. Mecking, and R. Wood, 2015: Global and european climate impacts of a slowdown of the AMOC in a high resolution GCM. *Climate dynamics*, **45 (11)**, 3299–3316.

James, R., R. Washington, C.-F. Schleussner, J. Rogelj, and D. Conway, 2017: Characterizing half-a-degree difference: a review of methods for identifying regional climate responses to global warming targets. *Wiley Interdisciplinary Reviews: Climate Change*, **8 (2)**, e457.

Josey, S. A., J. J.-M. Hirschi, B. Sinha, A. Duchez, J. P. Grist, and R. Marsh, 2018: The recent Atlantic cold anomaly: Causes, consequences, and related phenomena. *Annual Review of Marine Science*, **10**, 475–501.

Kelley, M., and Coauthors, 2020: GISS-E2. 1: Configurations and climatology. *Journal of Advances in Modeling Earth Systems*, **12 (8)**, e2019MS002 025.

Lachmy, O., and T. Shaw, 2018: Connecting the energy and momentum flux response to climate change using the Eliassen-Palm relation. *Journal of Climate*, **31 (18)**, 7401–7416.

Lau, N.-C., H. Tennekes, and J. M. Wallace, 1978: Maintenance of the momentum flux by transient eddies in the upper troposphere. *Journal of Atmospheric Sciences*, **35 (1)**, 139–147.

Levine, X. J., and T. Schneider, 2011: Response of the Hadley circulation to climate change in an aquaplanet GCM coupled to a simple representation of ocean heat transport. *Journal of the Atmospheric Sciences*, **68 (4)**, 769–783.

Lim, G. H., and J. M. Wallace, 1991: Structure and evolution of baroclinic waves as inferred from regression analysis. *Journal of Atmospheric Sciences*, **48 (15)**, 1718–1732.

Liu, W., A. V. Fedorov, S.-P. Xie, and S. Hu, 2020: Climate impacts of a weakened Atlantic Meridional Overturning Circulation in a warming climate. *Science advances*, **6 (26)**, eaaz4876.

Lu, J., G. A. Vecchi, and T. Reichler, 2007: Expansion of the hadley cell under global warming. *Geophysical Research Letters*, **34 (6)**.

Magnusdottir, G., and R. Saravannan, 1999: The response of atmospheric heat transport to zonally-averaged SST trends. *Tellus A: Dynamic Meteorology and Oceanography*, **51 (5)**, 815–832.

Marshall, J., J. R. Scott, K. C. Armour, J.-M. Campin, M. Kelley, and A. Romanou, 2015: The ocean's role in the transient response of climate to abrupt greenhouse gas forcing. *Climate Dynamics*, **44 (7)**, 2287–2299.

Meinshausen, M., and Coauthors, 2020: The shared socio-economic pathway (SSP) greenhouse gas concentrations and their extensions to 2500. *Geoscientific Model Development*, **13 (8)**, 3571–3605.

Menary, M. B., and R. A. Wood, 2018: An anatomy of the projected North Atlantic warming hole in CMIP5 models. *Climate Dynamics*, **50 (7)**, 3063–3080.

Menzel, M. E., D. Waugh, and K. Grise, 2019: Disconnect between Hadley cell and subtropical jet variability and response to increased CO_2. *Geophysical Research Letters*, **46 (12)**, 7045–7053.

Miller, R. L., and Coauthors, 2021: CMIP6 historical simulations (1850–2014) with GISS-E2. 1. *Journal of Advances in Modeling Earth Systems*, **13 (1)**, e2019MS002 034.

Mitevski, I., C. Orbe, R. Chemke, L. Nazarenko, and L. M. Polvani, 2021: Non-monotonic response of the climate system to abrupt CO_2 forcing. *Geophysical research letters*, **48 (6)**, e2020GL090 861.

Mitevski, I., L. M. Polvani, and C. Orbe, 2022: Asymmetric warming/cooling response to CO_2 increase/decrease mainly due to non-logarithmic forcing, not feedbacks. *Geophysical Research Letters*, **49 (5)**, e2021GL097 133.

Nazarenko, L. S., and Coauthors, 2022: Future climate change under SSP emission scenarios with GISS-E2. 1. *Journal of Advances in Modeling Earth Systems*, e2021MS002871.

Orbe, C., and Coauthors, 2020: GISS model E2. 2: A climate model optimized for the middle atmosphere—2. Validation of large-scale transport and evaluation of climate response. *Journal of Geophysical Research: Atmospheres*, **125 (24)**, e2020JD033 151.

O'Reilly, C. H., M. Huber, T. Woollings, and L. Zanna, 2016: The signature of low-frequency oceanic forcing in the Atlantic Multidecadal Oscillation. *Geophysical Research Letters*, **43 (6)**, 2810–2818.

Orihuela-Pinto, B., M. H. England, and A. S. Taschetto, 2022: Interbasin and interhemispheric impacts of a collapsed Atlantic Overturning Circulation. *Nature Climate Change*, 1–8.

Outten, S., I. Esau, and O. H. Otterå, 2018: Bjerknes compensation in the CMIP5 climate models. *Journal of Climate*, **31 (21)**, 8745–8760.

Pedro, J. B., M. Jochum, C. Buizert, F. He, S. Barker, and S. O. Rasmussen, 2018: Beyond the bipolar seesaw: Toward a process understanding of interhemispheric coupling. *Quaternary Science Reviews*, **192**, 27–46.

Rahmstorf, S., J. E. Box, G. Feulner, M. E. Mann, A. Robinson, S. Rutherford, and E. J. Schaffernicht, 2015: Exceptional twentieth-century slowdown in Atlantic Ocean overturning circulation. *Nature climate change*, **5 (5)**, 475–480.

Rind, D., G. A. Schmidt, J. Jonas, R. Miller, L. Nazarenko, M. Kelley, and J. Romanski, 2018: Multicentury instability of the Atlantic meridional circulation in rapid warming simulations with GISS ModelE2. *Journal of Geophysical Research: Atmospheres*, **123 (12)**, 6331–6355.

Rind, D., and Coauthors, 2020: GISS Model E2. 2: A climate model optimized for the middle atmosphere—Model structure, climatology, variability, and climate sensitivity. *Journal of Geophysical Research: Atmospheres*, **125 (10)**, e2019JD032 204.

Robson, J., P. Ortega, and R. Sutton, 2016: A reversal of climatic trends in the North Atlantic since 2005. *Nature Geoscience*, **9 (7)**, 513–517.

Romanou, A., and Coauthors, Under Review: Stochastic bifurcation of the North Atlantic circulation under a mid-range future climate scenario with the NASA-GISS ModelE. *Journal of Climate*.

Samset, B., and Coauthors, 2016: Fast and slow precipitation responses to individual climate forcers: A pdrmip multimodel study. *Geophysical research letters*, **43 (6)**, 2782–2791.

Santer, B. D., T. M. Wigley, M. E. Schlesinger, and J. F. Mitchell, 1990: Developing climate scenarios from equilibrium GCM results.

Schmidt, D. F., and K. M. Grise, 2017: The response of local precipitation and sea level pressure to Hadley cell expansion. *Geophysical Research Letters*, **44 (20)**, 10–573.

Schneider, T., 2006: The general circulation of the atmosphere. *Annu. Rev. Earth Planet. Sci.*, **34**, 655–688.

Shaffrey, L., and R. Sutton, 2006: Bjerknes compensation and the decadal variability of the energy transports in a coupled climate model. *Journal of Climate*, **19 (7)**, 1167–1181.

Shaw, T., and A. Voigt, 2015: Tug of war on summertime circulation between radiative forcing and sea surface warming. *Nature Geoscience*, **8 (7)**, 560–566.

Shepherd, T. G., 2014: Atmospheric circulation as a source of uncertainty in climate change projections. *Nature Geoscience*, **7 (10)**, 703–708.

Smith, D. M., R. Eade, N. J. Dunstone, D. Fereday, J. M. Murphy, H. Pohlmann, and A. A. Scaife, 2010: Skilful multi-year predictions of Atlantic hurricane frequency. *Nature geoscience*, **3 (12)**, 846–849.

Tebaldi, C., and J. M. Arblaster, 2014: Pattern scaling: Its strengths and limitations, and an update on the latest model simulations. *Climatic Change*, **122 (3)**, 459–471.

Thompson, D. W., and T. Birner, 2012: On the linkages between the tropospheric isentropic slope and eddy fluxes of heat during Northern Hemisphere winter. *Journal of the atmospheric sciences*, **69 (6)**, 1811–1823.

Timmermann, A., and Coauthors, 2007: The influence of a weakening of the Atlantic meridional overturning circulation on ENSO. *Journal of climate*, **20 (19)**, 4899–4919.

Vallis, G. K., P. Zurita-Gotor, C. Cairns, and J. Kidston, 2015: Response of the large-scale structure of the atmosphere to global warming. *Quarterly Journal of the Royal Meteorological Society*, **141 (690)**, 1479–1501.

Vellinga, M., and R. A. Wood, 2008: Impacts of thermohaline circulation shutdown in the twenty-first century. *Climatic Change*, **91 (1)**, 43–63.

Vial, J., C. Cassou, F. Codron, S. Bony, and Y. Ruprich-Robert, 2018: Influence of the Atlantic meridional overturning circulation on the tropical climate response to CO_2 forcing. *Geophysical Research Letters*, **45 (16)**, 8519–8528.

Waugh, D. W., and Coauthors, 2018: Revisiting the relationship among metrics of tropical expansion. *Journal of Climate*, **31 (18)**, 7565–7581.

Weijer, W., W. Cheng, O. A. Garuba, A. Hu, and B. Nadiga, 2020: CMIP6 models predict significant 21st century decline of the Atlantic meridional overturning circulation. *Geophysical Research Letters*, **47 (12)**, e2019GL086 075.

Woollings, T., J. M. Gregory, J. G. Pinto, M. Reyers, and D. J. Brayshaw, 2012: Response of the North Atlantic storm track to climate change shaped by ocean–atmosphere coupling. *Nature Geoscience*, **5 (5)**, 313–317.

Wu, L., C. Li, C. Yang, and S.-P. Xie, 2008: Global teleconnections in response to a shutdown of the Atlantic meridional overturning circulation. *Journal of Climate*, **21 (12)**, 3002–3019.

Zappa, G., and T. G. Shepherd, 2017: Storylines of atmospheric circulation change for european regional climate impact assessment. *Journal of Climate*, **30 (16)**, 6561–6577.

Zhang, R., and T. L. Delworth, 2005: Simulated tropical response to a substantial weakening of the Atlantic thermohaline circulation. *Journal of climate*, **18 (12)**, 1853–1860.

Zhang, R., and T. L. Delworth, 2006: Impact of Atlantic multidecadal oscillations on India/Sahel rainfall and Atlantic hurricanes. *Geophysical research letters*, **33 (17)**.

Zhang, R., S. M. Kang, and I. M. Held, 2010: Sensitivity of climate change induced by the weakening of the Atlantic meridional overturning circulation to cloud feedback. *Journal of Climate*, **23 (2)**, 378–389.